Nonlinear static response analysis of sandwich beams using the Refined Zigzag Theory

NONLINEAR STATIC RESPONSE ANALYSIS OF SANDWICH BEAMS USING THE REFINED ZIGZAG THEORY

Alessia Ascione, Marco Gherlone

Abstract

The Refined Zigzag Theory (RZT) is assessed for the buckling and nonlinear static response analysis of multilayered composite and sandwich beams. A nonlinear formulation of the RZT is developed taking into account geometric imperfections and nonlinearities using the Von Kármán nonlinear strain-displacement relations. FE analyses are conducted employing C^0-beam elements based on the RZT and the Timoshenko Beam Theory (TBT) to model three sandwich beams with different core materials and slenderness ratios, in both simply supported and cantilever configurations. The reference solutions are obtained by high-fidelity FE commercial codes, Abaqus® and Nastran®. The first two buckling loads are evaluated for the beams without initial imperfections. Several shapes are then assumed as geometric imperfections to calculate the beams nonlinear response to axial-compressive loads. The comparisons show the very high accuracy of the RZT (comparable to high-fidelity FE commercial codes) for both the buckling and nonlinear static

Politecnico di Torino, Department of Mechanical and Aerospace Engineering, Corso Duca degli Abruzzi 24, 1029 Torino (Italy)

Corresponding author: Alessia Ascione, Politecnico di Torino, Department of Mechanical and Aerospace Engineering, Corso Duca degli Abruzzi 24, 1029 Torino (Italy), e-mail: alessia.ascione@polito.it

analyses and its superior capability with respect to the TBT to deal with sandwich beams with low slenderness ratio and higher face-to-core stiffness ratio.

1. Introduction

In the last sixty years, the usage of multilayered composite and sandwich materials has significantly increased in civil, mechanical and aerospace engineering applications. The percentage of composites and sandwiches employed in airplane structures has risen from 2% to more than 50% in modern aircrafts [1]. The main advantages of such materials are the good resistance to corrosion, the high stiffness-to-weight and strength-to-weight ratios and the "tailoring" freedom related to the possibility to obtain optimal structural responses by adopting selected stacking sequences. These properties make multilayered composite structures very attractive, especially for primary structural components of aircrafts. In working conditions, a large proportion of an aircraft's structure is subjected to axial and bending loads and the buckling is one of the most typical failure modes. The buckling is a nonlinear phenomenon associated with large transverse displacements when a small load increment (with respect to a critical level) is added to the axial compressive or shear load applied to a beam- or plate-like structure. An accurate understanding of this phenomenon in metal structures allows the usage of such structures also in the post-buckling regime, leading to a considerable reduction of the thicknesses required to carry the applied loads. On the other hand, composites and sandwiches are still used only in the pre-buckling regime because their behavior still cannot be predicted with high accuracy in critical situations. As a consequence, one of the major challenges for the aerospace industries is the possibility to employ composites in post-buckling regime to further reduce the structural weight [1].

Various approaches have been adopted for predicting critical buckling loads in structural members usually subjected to compressive loads. In some of these approaches, geometric imperfections are also considered. Geometric imperfections taken into account are usually related to initial deviations from a straight beam axis configuration (pre-deflections). In other words, perfect beams are those

with an initially straight axis configuration. In [2], Brush and Almroth collected the most common methods and investigated the stability of structures considering geometric nonlinearities in the elementary bending analysis. A first attempt to analyze the behavior of composite and sandwich beams was conducted applying the Classical Lamination Theory (CLT) and the classical theory for beams (Bernoulli-Euler beam theory). As an example, Barbero and Raftoyiannis [3] evaluated the critical buckling loads and the failure modes of pultruded composite columns with thin-walled cross sections, employing the CLT for the stiffness characteristics and then the Euler's critical load formula. Columns of various lengths were considered to investigate the transition of the first failure mode from global to local buckling when the beam length decreases. The classical theory was also adopted to investigate the nonlinear behavior of composite beams with geometric imperfections both in pre- and post-buckling regimes. In [4], the effect of piezoelectric layers attached to the beam was included in the nonlinear formulation of Bernoulli-Euler beam theory for initially imperfect composite beams under compression. The analysis showed that the nonlinear response of slender composite beams in the pre-buckling regime can be significantly modified by the piezoelectric actuation, obtaining a load-displacement equilibrium path that is close to the ideal solution for perfect beams. Emam and Nayfeh [5] found a closed form solution for the equilibrium configurations of composite beams loaded beyond the critical buckling load and studied both the stability in post-buckling regime and the dynamic behavior in the buckled state considering various boundary conditions. The mathematical model was based on the Bernoulli-Euler beam theory.

However, many authors demonstrated the inaccuracy of this theory for the analyses of multilayered composite and sandwich structures. Khedir and Reddy in [6] showed that the Bernoulli-Euler beam theory highly overestimates the buckling loads of cross-ply laminated beams. They compared the exact analytical solutions of the governing equations for the buckling analysis based on four different theories: the Bernoulli-Euler beam theory, the Timoshenko beam theory (or First-order Shear Deformation Theory, FSDT), the Second-Order Shear Deformation Theory (SSDT) and the Reddy-Third order Shear Deformation Theory (TSDT). The critical loads evaluated with the shear-

deformation theories were rather similar to one another but much lower than Bernoulli-Euler values. A nonlinear formulation of the Reddy TSDT was developed in [7] to study the pre- and post-buckling of imperfect laminated beams. The governing equations were solved numerically for different types of boundary conditions to evaluate the equilibrium path of longitudinal and transverse displacements when the axial-compressive load increases from zero beyond the buckling load. Various imperfection functions and lay-ups were considered for investigating their effect on the structural behavior in post-buckling regime. In [8-10], shear deformation theories of various orders were employed to study the stability of composite laminates and functionally-graded material (FGM) plates under thermal loads. Accurate predictions of the critical temperature were obtained even using theories based on four kinematic variables. Higher-order and trigonometric shear deformation theories based on a number of unknowns lower than conventional theories were developed also for the static and free vibration analysis of FGM plates [11-19]. The maximum deflection and the natural frequencies were accurately calculated by theories based on four variables and involving the temperature [11-14] and moisture [15,16] effects, and by five-variable theories able to model also the thickness stretching [17-19].

The importance of the shear deformation in the buckling and post-buckling analysis, especially for composite and sandwich structures, was observed also by Sheinman. In [20], he developed a nonlinear formulation based on a TSDT to investigate the post-buckling behavior of laminated beams, showing that not only the shear deformation must be considered in composite beam analyses but also that a higher-order theory is necessary when the beam length-to-thickness ratio is low. However, Tessler et al. observed that the FSDT and the HSDTs (Higher-order Shear Deformation Theories), which belong to a class of theories called *Equivalent-Single Layer* (ESL), can lead to erroneous predictions of the in-plane and transverse-shear stresses in case of either thick beams (or plates) or highly heterogeneous material lay-ups [21-26]. The major drawback of these theories is the through-the thickness discontinuity of the transverse stresses as a consequence of a C^1-continuous displacement field assumption. *Layer-Wise* (LW) theories overcome these problems

assuming an independent displacement field for each layer and enforcing the stress continuity at layer interfaces. They are able to accurately reproduce the zigzag pattern along the thickness of the in-plane displacements, but their computational cost is affordable only in case of few material layers [27, 28]. A compromise between the ESL and the LW theories in terms of accuracy and computational effort is represented by the *zigzag theories*, where the displacement field is developed in such a way that the transverse shear stresses continuity is ensured and the numbers of kinematic variables is independent of the number of layers [29, 30]. Among this class of theories, the Refined Zigzag Theory (RZT) [21-26], has proven to be one of the most amenable to engineering practice because of its superior capacity to predict static, dynamic and buckling behavior of composite and sandwich structures, including very thick laminates with highly heterogeneous material properties, with very low computational cost. In [25], RZT was compared to TSDT and a HSDT for the static, free-vibration and buckling analysis of sandwich plates, showing better performances. The promising characteristics of the RZT has led to an interest in extending the theory to the nonlinear analysis of composite and sandwich beams under axial-compressive loads.

Aim of the present effort is to assess the Refined Zigzag Theory for the buckling and nonlinear response analysis of composite and sandwich beams also in presence of geometric imperfections. At first, a nonlinear formulation of RZT for beams has been developed using Von Kàrmàn strain-displacement relations. The nonlinear response of geometrically imperfect composite and sandwich beams in the pre-buckling regime can be modelled. A finite element approximation based on RZT C^0-beam elements [24] has been introduced to solve the nonlinear equilibrium equations for any kind of boundary conditions. The RZT capability to solve this kind of problems has been assessed by comparison with high fidelity, two-dimensional Abaqus® and MSC/Nastran® FE models, for simply-supported and cantilevered sandwich beams.

2. Nonlinear formulation of the Refined Zigzag Theory for geometrically imperfect beams

In this section, a nonlinear formulation of the Refined Zigzag Theory for geometrically imperfect beams is developed.

2.1 Displacements, strains, and stresses

Consider a beam of length L and cross-sectional area $A = 2h\,x\,b$, where $2h$ is the total thickness and b the cross-sectional width. The beam is composed of N orthotropic material layers perfectly bonded to each other (Figure 1); each layer is denoted by the superscript (k).

[insert Figure 1.]

The longitudinal axis of the beam is denoted by x, with $x \in [x_a, x_b]$ ($L = x_b - x_a$), whereas the thickness coordinate is z, with $z \in [-h, h]$. The thickness of the k th layer is $2h^{(k)}$ and its thickness coordinate ranges from $z_{(k-1)}$ to $z_{(k)}$ (Figure 2a). It is assumed that the beam can be deformed only in the (x,z) plane. Distributed loads (units of force/length) are applied at the bottom $(z = -h)$ and top $(z = +h)$ beam surfaces; namely, the axial, $p^b(x)$ and $p^t(x)$, and transverse, $q^b(x)$ and $q^t(x)$, loads. The end cross-sections are subjected to the action of prescribed axial (T_{xa}, T_{xb}) and transverse shear (T_{za}, T_{zb}) tractions (Figure 1).

The orthogonal components of the displacement vector of the Refined Zigzag Theory can be written in the following matrix form [24]

$$\begin{Bmatrix} u_x^{(k)}(x,z) \\ u_z(x,z) \end{Bmatrix} = \begin{bmatrix} 1 & 0 & z & \phi^{(k)}(z) \\ 0 & 1 & 0 & 0 \end{bmatrix} \begin{Bmatrix} u(x) \\ w(x) \\ \vartheta(x) \\ \psi(x) \end{Bmatrix} \equiv \mathbf{Z}_{\mathbf{u}}(z)\mathbf{u}(x) \tag{1}$$

where $u_x^{(k)}$ and u_z are the displacements in the directions of the x and z -axis, respectively, and $\mathbf{u}$

is a vector containing the four kinematic variables of the theory: the uniform axial displacement, $u(x)$, the deflection, $w(x)$, the average cross-sectional (bending) rotation, $\vartheta(x)$, and the *zigzag rotation*, $\psi(x)$. Note that $u_z = w(x)$ is through-the-thickness uniform hence the superscript (k) does not appear in the notation for this quantity. Moreover, $\psi(x)$ is the RZT additional kinematic variable with respect to the Timoshenko beam theory and measures the magnitude of the zigzag contribution to the axial displacement, $\phi^{(k)}(z)\psi(x)$, i.e., the cross-sectional piecewise continuous distortion typical of multilayered structures.

The zigzag function, $\phi^{(k)} = \phi^{(k)}(z)$, has units of length, is a piecewise linear, C^0-continuous function of the thickness coordinate and is completely defined once its $(N+1)$ interfacial values $\phi_{(i)}(i = 0,1,\ldots,N)$ are known (see Figure 2b).

[insert Figure 2.]

$\phi^{(k)}$ is set to vanish on the top and bottom laminate surface, i.e., $\phi_{(0)} \equiv \phi^{(1)}(z_{(0)}) = 0$ and $\phi_{(N)} \equiv \phi^{(N)}(z_{(N)}) = 0$. The internal values, $\phi_{(j)} \equiv \phi^{(j)}(z_{(j)}) = \phi^{(j+1)}(z_{(j)})$ $(j = 1,2,\ldots,N-1)$ can be obtained as follows

$$\phi_{(j)} = \phi_{(j-1)} + 2h^{(j)}\beta^{(j)} \quad (j = 1,2,...,N-1) \tag{2}$$

where $\beta^{(k)}$ is the zigzag function slope in each layer. $\beta^{(k)}$ can be obtained by using the following expression

$$\beta^{(k)} \equiv \phi_{,z}^{(k)} = \frac{G}{G_{xz}^{(k)}} - 1 \quad (k = 1,2,...,N) \tag{3}$$

where $G_{xz}^{(k)}$ is the kth layer transverse shear modulus and G denotes a weighted-average transverse shear modulus of the laminate

$$G \equiv \left(\frac{1}{2h} \int_{-h}^{+h} \frac{dz}{G_{xz}^{(k)}} \right)^{-1} = \left(\frac{1}{h} \sum_{k=1}^{N} \frac{h^{(k)}}{G_{xz}^{(k)}} \right)^{-1} \tag{4}$$

The complete derivation of Eqs. (2)-(4) can be found in [21].

Geometric imperfections and nonlinearity are included in the model by considering the Von Kármán nonlinear strain-displacement relations

$$\begin{aligned} \varepsilon_x &= u_{x,x} + \frac{1}{2} u_{z,x}^2 + u_{z,x} w_{,x}^* \\ \gamma_{xz} &= u_{x,z} + u_{z,x} \end{aligned} \tag{5}$$

where the function w^* describes initial imperfections, i.e. initial stress-free transverse deviations from a straight axis configuration (see Figure 1). Considering that only planar deformations in the (x,z) plane are investigated, geometric imperfections are assumed to occur in the same plane. Substituting the displacement components (Eq. (1)) into Eq. (5), the following nonlinear strains for the Refined Zigzag Theory are obtained

$$\begin{aligned}\varepsilon_x^{(k)}(x,z) &= u_{,x}(x) + z\theta_{,x}(x) + \phi^{(k)}(z)\psi_{,x}(x) + \frac{1}{2}w_{,x}^2(x) + w_{,x}(x)w_{,x}^*(x) \\ &= \mathbf{Z}_{\boldsymbol{\varepsilon}}^{(\mathbf{k})}(z)\boldsymbol{\omega}(x) + \frac{\mathbf{1}}{\mathbf{2}}\boldsymbol{\omega}(x)^T\mathbf{H}\boldsymbol{\omega}(x) + \boldsymbol{\omega}^*(x)^T\boldsymbol{\omega}(x) \\ \gamma_{xz}^{(k)}(x,z) &= w_{,x}(x) + \theta(x) + \beta^{(k)}\psi(x) \\ &= \mathbf{Z}_{\boldsymbol{\gamma}}^{(\mathbf{k})}(z)\boldsymbol{\omega}(x)\end{aligned} \tag{6}$$

where

$$\begin{aligned}\boldsymbol{\omega} &\equiv \begin{bmatrix} u_{,x} & w_{,x} & \vartheta & \psi & \vartheta_{,x} & \psi_{,x} \end{bmatrix}^T \\ \boldsymbol{\omega}^* &\equiv \begin{bmatrix} 0 & w_{,x}^* & 0 & 0 & 0 & 0 \end{bmatrix}^T\end{aligned} \tag{7}$$

The zero-one matrix $\mathbf{H}$ and the matrices $\mathbf{Z}_{\boldsymbol{\varepsilon}}^{(\mathbf{k})}$ and $\mathbf{Z}_{\boldsymbol{\gamma}}^{(\mathbf{k})}$ (function of the thickness coordinate) are defined in Appendix A.

The material of each layer is linearly elastic and orthotropic, with the orthotropy directions corresponding to the axes of the coordinate system, (x, y, z). A plane-stress behavior is assumed in the (x, z) plane. Moreover, the transverse normal stress, $\sigma_z^{(k)}$, is negligible with respect to the axial and transverse shear stresses. Consequently, the constitutive equations for the *k*th layer are

$$\begin{aligned}\sigma_x^{(k)} &= E_x^{(k)}\varepsilon_x^{(k)} \\ \tau_{xz}^{(k)} &= G_{xz}^{(k)}\gamma_{xz}^{(k)}\end{aligned} \tag{8}$$

where $E_x^{(k)}$ and $G_{xz}^{(k)}$ are, respectively, the Young modulus along the x-direction and the transverse-shear modulus in the (x, z) plane.

2.2 Principle of Virtual Works

The Principle of Virtual Works (PVW) is employed to derive the Euler–Lagrange equilibrium equations and the set of consistent boundary conditions. The PVW is written in the form

$$\delta U - \delta L_e = 0 \tag{9}$$

where U is the strain energy and L_e is the work done by external forces. Introducing the vectors of strain and stress components as $\boldsymbol{\varepsilon} \equiv [\varepsilon_x^{(k)} \quad \gamma_{xz}^{(k)}]^T$ and $\boldsymbol{\sigma} \equiv [\sigma_x^{(k)} \quad \tau_{xz}^{(k)}]^T$, the virtual variation of U is

$$\delta U = \int_V \boldsymbol{\delta\varepsilon}^T \boldsymbol{\sigma} dv = \int_{x_a}^{x_b} \int_A \left[\delta\varepsilon_x^{(k)} \sigma_x^{(k)} + \delta\gamma_{xz}^{(k)} \tau_{xz}^{(k)} \right] dA dx \tag{10}$$

For the loading conditions represented in Figure 1

$$\begin{aligned} \delta L_e = & \int_{x_a}^{x_b} \left[\delta u_x^{(1)}(-h) p^b + \delta u_x^{(N)}(+h) p^t + \delta u_z^{(1)}(-h) q^b + \delta u_z^{(N)}(+h) q^t \right] dx \\ & - \int_A \left[\delta u_x^{(k)}(x_a, z) T_{xa} + \delta u_z(x_a, z) T_{za} \right] dA + \int_A \left[\delta u_x^{(k)}(x_b, z) T_{xb} + \delta u_z(x_\beta, z) T_{zb} \right] dA \end{aligned} \tag{11}$$

Eqs. (6) and (8) are now substituted into Eq. (10). The latter, together with Eq. (11), is then substituted into Eq. (9). Integrating over the beam's cross-section yields a one-dimensional form of the PVW based on the nonlinear formulation of RZT

$$\begin{aligned} & \int_{x_a}^{x_b} \left[N_x \delta(u_{,x} + \frac{1}{2} w_{,x}^2 + w_{,x} w_{,x}^*) + M_x \delta\theta_{,x} + V_x \delta(w_{,x} + \theta) + M_\phi \delta\psi_{,x} + V_\phi \delta\psi - p\delta u - q\delta w - m\delta\theta \right] dx \\ & + \left[\bar{N}_{xa} \delta u(x_a) + \bar{M}_{xa} \delta\theta(x_a) + \bar{V}_{xa} \delta w(x_a) + \bar{M}_{\phi a} \delta\psi(x_a) \right] \\ & - \left[\bar{N}_{xb} \delta u(x_b) + \bar{M}_{xb} \delta\theta(x_b) + \bar{V}_{xb} \delta w(x_b) + \bar{M}_{\phi b} \delta\psi(x_b) \right] = 0 \end{aligned} \tag{12}$$

where

$$\left[N_x, M_x, M_\phi, V_x, V_\phi\right] \equiv \int_A \left[\sigma_x^{(k)}, z\sigma_x^{(k)}, \phi^{(k)}\sigma_x^{(k)}, \tau_{xz}^{(k)}, \beta^{(k)}\tau_{xz}^{(k)}\right] dA \tag{13.1}$$

$$\left[\bar{N}_{x\alpha}, \bar{M}_{x\alpha}, \bar{M}_{\phi\alpha}, \bar{V}_{x\alpha}\right] \equiv \int_A \left[T_{x\alpha}, zT_{x\alpha}, \phi^{(k)}T_{x\alpha}, T_{z\alpha}\right] dA, \quad (\alpha = a,b) \tag{13.2}$$

are the internal and applied stress resultant forces and moments, respectively, and

$$\left[p, q, m\right] \equiv \left[\left(p^b + p^t\right), \left(q^b + q^t\right), \left(h\left(p^t - p^b\right)\right)\right] \tag{14}$$

are the resultant distributed loads.

Starting from definition (13.1) and making use of Eqs. (6) and (8), the nonlinear constitutive equations for the RZT imperfect beam are obtained and summarized in the following matrix form

$$\mathbf{R} = \boldsymbol{\Delta}\boldsymbol{\omega} + \bar{\boldsymbol{\Delta}}\left(\frac{1}{2}\boldsymbol{\omega}^{\mathrm{T}}\mathbf{H}\boldsymbol{\omega} + \boldsymbol{\omega}^{*T}\boldsymbol{\omega}\right) \tag{15}$$

where $\mathbf{R} \equiv \left[N_x \quad V_x \quad V_\phi \quad M_x \quad M_\phi\right]^T$, $\boldsymbol{\Delta}$ is the matrix containing the stiffness coefficients and $\bar{\boldsymbol{\Delta}}$ is the first column of the matrix $\boldsymbol{\Delta}$. Refer to Appendix A for the definition of $\boldsymbol{\Delta}$.

Integration by parts of Eq. (12) yields the nonlinear equilibrium equations in terms of resultant forces and moments

$$
\begin{aligned}
&N_{x,x} + p = 0 \\
&V_{x,x} + \left[N_x \left(w_{,x} + w^*_{,x} \right) \right]_{,x} + q = 0 \\
&M_{x,x} - V_x + m = 0 \\
&M_{\phi,x} - V_\phi = 0
\end{aligned}
\tag{16}
$$

and a set of consistent boundary conditions (geometric and kinetic, respectively)

$$
\begin{aligned}
&\text{either } u(x_\alpha) = \bar{u}_\alpha \text{ or } N_x(x_\alpha) = \bar{N}_{x\alpha} \\
&\text{either } w(x_\alpha) = \bar{w}_\alpha \text{ or } V_x(x_\alpha) = \bar{V}_{x\alpha} \\
&\text{either } \vartheta(x_\alpha) = \bar{\vartheta}_\alpha \text{ or } M_x(x_\alpha) = \bar{M}_{x\alpha} \\
&\text{either } \psi(x_\alpha) = \bar{\psi}_\alpha \text{ or } V_\phi(x_\alpha) = \bar{M}_{\phi\alpha}
\end{aligned}
\tag{17}
$$

where the quantities denoted by an overbar are the kinematic variables and the stress resultants prescribed at the beam ends, $x_\alpha \equiv (x_a, x_b)$. Substituting Eqs. (15) into Eqs. (16), the equilibrium equations can be expressed in terms of displacement components

$$
\begin{aligned}
&A_{11}\left[u_{,xx} + \left(\frac{1}{2} w_{,x}{}^2 + w_{,x} w^*_{,x} \right)_{,x} \right] + B_{12}\theta_{,xx} + B_{13}\psi_{,xx} + p = 0 \\
&\bar{G}A\left(w_{,xx} + \theta_{,x} \right) + \left(G - \bar{G} \right) A\psi_{,x} + \left\{ \left[A_{11}\left[u_{,x} + \left(\frac{1}{2} w_{,x}{}^2 + w_{,x} w^*_{,x} \right) \right] + B_{12}\theta_{,x} + B_{13}\psi_{,x} \right] \left(w_{,x} + w^*_{,x} \right) \right\}_{,x} + q = 0 \\
&B_{12}\left[u_{,xx} + \left(\frac{1}{2} w_{,x}{}^2 + w_{,x} w^*_{,x} \right)_{,x} \right] + D_{11}\theta_{,xx} + D_{12}\psi_{,xx} - \bar{G}A\left(w_{,x} + \theta \right) - \left(G - \bar{G} \right) A\psi + m = 0 \\
&B_{13}\left[u_{,xx} + \left(\frac{1}{2} w_{,x}{}^2 + w_{,x} w^*_{,x} \right)_{,x} \right] + D_{12}\theta_{,xx} + D_{22}\psi_{,xx} - \left(G - \bar{G} \right) A\left(w_{,x} + \theta \right) - \left(\bar{G} - G \right) A\psi = 0
\end{aligned}
\tag{18}
$$

where the stiffness coefficients are defined in Appendix A.

An approximate solution of Eqs. (18) is now obtained for general boundary and loading conditions by means of the finite element method.

3. Finite element formulation

Before introducing the finite element approximation into the PVW statement, the strain energy virtual variation δU , Eq. (10), is expressed as a function of $\boldsymbol{\omega}$ and $\boldsymbol{\omega}^*$ by using Eqs. (6)-(8). After some straightforward operations and neglecting higher order terms, the following expression is obtained

$$\begin{aligned}\delta U = &\int_{x_a}^{x_b}\int_A \left[\delta\boldsymbol{\omega}^T \mathbf{Z}_{\boldsymbol{\varepsilon}}^{(\mathbf{k})T} E_x^{(k)} \mathbf{Z}_{\boldsymbol{\varepsilon}}^{(\mathbf{k})} \boldsymbol{\omega}\right] dA dx + \frac{1}{2}\int_{x_a}^{x_b}\int_A \left[\delta\boldsymbol{\omega}^T \mathbf{Z}_{\boldsymbol{\varepsilon}}^{(\mathbf{k})T} E_x^{(k)} \boldsymbol{\omega}^T \mathbf{H}\boldsymbol{\omega}\right] dA dx \\ &+\int_{x_a}^{x_b}\int_A \left[\delta\boldsymbol{\omega}^T \mathbf{Z}_{\boldsymbol{\varepsilon}}^{(\mathbf{k})T} E_x^{(k)} \boldsymbol{\omega}^{*T} \boldsymbol{\omega}\right] dA dx + \int_{x_a}^{x_b}\int_A \left[\delta\boldsymbol{\omega}^T \mathbf{H}\boldsymbol{\omega} E_x^{(k)} \mathbf{Z}_{\boldsymbol{\varepsilon}}^{(\mathbf{k})} \boldsymbol{\omega}\right] dA dx \\ &+\int_{x_a}^{x_b}\int_A \left[\delta\boldsymbol{\omega}^T \boldsymbol{\omega}^* E_x^{(k)} \mathbf{Z}_{\boldsymbol{\varepsilon}}^{(\mathbf{k})} \boldsymbol{\omega}\right] dA dx + \int_{x_a}^{x_b}\int_A \left[\delta\boldsymbol{\omega}^T \mathbf{Z}_{\boldsymbol{\gamma}}^{(\mathbf{k})T} G_{xz}^{(k)} \mathbf{Z}_{\boldsymbol{\gamma}}^{(\mathbf{k})} \boldsymbol{\omega}\right] dA dx\end{aligned} \tag{19}$$

Since $\boldsymbol{\omega}$, $\boldsymbol{\omega}^*$ and $\mathbf{H}$ do not depend on the cross-sectional coordinate axes, the following expression for δU can be obtained from Eq. (19)

$$\begin{aligned}\delta U = &\int_{x_a}^{x_b} \delta\boldsymbol{\omega}^T \int_A \left[\mathbf{Z}_{\boldsymbol{\varepsilon}}^{(\mathbf{k})T} E_x^{(k)} \mathbf{Z}_{\boldsymbol{\varepsilon}}^{(\mathbf{k})}\right] dA\boldsymbol{\omega} dx + \frac{1}{2}\int_{x_a}^{x_b} \delta\boldsymbol{\omega}^T \int_A \left[\mathbf{Z}_{\boldsymbol{\varepsilon}}^{(\mathbf{k})T} E_x^{(k)}\right] dA\boldsymbol{\omega}^T \mathbf{H}\boldsymbol{\omega} dx \\ &+\int_{x_a}^{x_b} \delta\boldsymbol{\omega}^T \int_A \left[\mathbf{Z}_{\boldsymbol{\varepsilon}}^{(\mathbf{k})T} E_x^{(k)}\right] dA\boldsymbol{\omega}^{*T}\boldsymbol{\omega} dx + \int_{x_a}^{x_b} \delta\boldsymbol{\omega}^T \mathbf{H}\boldsymbol{\omega} \int_A \left[E_x^{(k)} \mathbf{Z}_{\boldsymbol{\varepsilon}}^{(\mathbf{k})}\right] dA\boldsymbol{\omega} dx \\ &+\int_{x_a}^{x_b} \delta\boldsymbol{\omega}^T \boldsymbol{\omega}^* \int_A \left[E_x^{(k)} \mathbf{Z}_{\boldsymbol{\varepsilon}}^{(\mathbf{k})}\right] dA\boldsymbol{\omega} dx + \int_{x_a}^{x_b} \delta\boldsymbol{\omega}^T \int_A \left[\mathbf{Z}_{\boldsymbol{\gamma}}^{(\mathbf{k})T} G_{xz}^{(k)} \mathbf{Z}_{\boldsymbol{\gamma}}^{(\mathbf{k})}\right] dA\boldsymbol{\omega} dx\end{aligned} \tag{19bis}$$

The kinematic variables are approximated within the beam finite element by using the *anisoparametric* interpolation [24]. In order to avoid shear locking, the deflection $w(x)$ is approximated using a quadratic polynomial whereas $u(x)$, $\vartheta(x)$ and $\psi(x)$ are linearly interpolated. A consistent constraining condition based on the resultant shear force V_x is used to simplify the element topology [24]: two nodes and four degrees of freedom per node are obtained (Figure 3).

[insert Figure 3.]

The matrix form of the element-wise approximation of the kinematic variables, $\mathbf{u}$, is

$$\mathbf{u} = \begin{Bmatrix} u(x) \\ w(x) \\ \vartheta(x) \\ \psi(x) \end{Bmatrix} \cong \mathbf{N}\mathbf{u}^{\mathbf{e}} \tag{20}$$

where $\mathbf{u}^{\mathbf{e}} \equiv \begin{bmatrix} u_1 & w_1 & \vartheta_1 & \psi_1 & u_2 & w_2 & \vartheta_2 & \psi_2 \end{bmatrix}^T$ is the vector of nodal degrees of freedom and $\mathbf{N}$ is the shape-function matrix (refer to [24] for details on the shape functions definition).

The initial imperfection function $w^*(x)$ is an input of the problem and is approximated within each element as a parabolic function

$$w^*(x) \cong \mathbf{N}_{\mathbf{w}}^* \mathbf{u}^{*\mathbf{e}} \tag{21}$$

where $\mathbf{N}_{\mathbf{w}}^*$ contains the Lagrange parabolic polynomials and $\mathbf{u}^{*\mathbf{e}} \equiv \begin{bmatrix} w_1^* & w_m^* & w_2^* \end{bmatrix}^T$ is the vector containing the values of the initial imperfection at the ends and at the mid-point of the element (Figure 4).

[insert Figure 4.]

The PVW statement is now discretized applying the finite element approximation to derive the element-level equilibrium equation corresponding to the nonlinear formulation of RZT. The vectors $\boldsymbol{\omega}$ and $\boldsymbol{\omega}^*$ are related to the corresponding nodal degrees-of-freedom vectors by the relations

$$\boldsymbol{\omega} = \mathbf{B}^{\mathbf{e}}\mathbf{u}^{\mathbf{e}}$$
$$\boldsymbol{\omega}^{*} = \mathbf{B}^{*\mathbf{e}}\mathbf{u}^{*\mathbf{e}} \tag{22}$$

where $\mathbf{B}^{\mathbf{e}}$ and $\mathbf{B}^{*\mathbf{e}}$ contain the derivatives with respect to the x-coordinate of the shape functions defined in Eq. (20) and Eq. (21), respectively (refer to Appendix B). The finite element approximation of the strain energy variation is obtained substituting Eq. (22) into Eq. (19bis)

$$\begin{aligned}\delta U \cong\ & \delta\mathbf{u}^{\mathbf{e}T}\int_0^{L_e}\mathbf{B}^{\mathbf{e}T}\cdot\int_A\left(\mathbf{Z}_{\boldsymbol{\varepsilon}}^{(\mathbf{k})T}E_x^{(k)}\mathbf{Z}_{\boldsymbol{\varepsilon}}^{(\mathbf{k})}\right)dA\cdot\mathbf{B}^{\mathbf{e}}dx\cdot\mathbf{u}^{\mathbf{e}}+\frac{1}{2}\delta\mathbf{u}^{\mathbf{e}T}\int_0^{L_e}\mathbf{B}^{\mathbf{e}T}\mathbf{Z}_{\mathbf{N}}^{\mathbf{e}T}\cdot\left[\mathbf{u}^{\mathbf{e}T}\mathbf{B}^{\mathbf{e}T}\mathbf{H}\mathbf{B}^{\mathbf{e}}\right]dx\cdot\mathbf{u}^{\mathbf{e}}\\ &+\delta\mathbf{u}^{\mathbf{e}T}\int_0^{L_e}\mathbf{B}^{\mathbf{e}T}\mathbf{Z}_{\mathbf{N}}^{\mathbf{e}T}\cdot\left[\mathbf{u}^{*\mathbf{e}T}\mathbf{B}^{*\mathbf{e}T}\mathbf{B}^{\mathbf{e}}\right]dx\cdot\mathbf{u}^{\mathbf{e}}+\delta\mathbf{u}^{\mathbf{e}T}\int_0^{L_e}\left[\mathbf{B}^{\mathbf{e}T}\mathbf{H}\mathbf{B}^{\mathbf{e}}\mathbf{u}^{\mathbf{e}}\right]\cdot\mathbf{Z}_{\mathbf{N}}^{\mathbf{e}}\mathbf{B}^{\mathbf{e}}dx\cdot\mathbf{u}^{\mathbf{e}}\\ &+\delta\mathbf{u}^{\mathbf{e}T}\int_0^{L_e}\left[\mathbf{B}^{\mathbf{e}T}\mathbf{B}^{*\mathbf{e}}\mathbf{u}^{*\mathbf{e}}\right]\cdot\mathbf{Z}_{\mathbf{N}}^{\mathbf{e}}\mathbf{B}^{\mathbf{e}}dx\cdot\mathbf{u}^{\mathbf{e}}+\delta\mathbf{u}^{\mathbf{e}T}\int_0^{L_e}\mathbf{B}^{\mathbf{e}T}\cdot\int_A\left(\mathbf{Z}_{\boldsymbol{\gamma}}^{(\mathbf{k})T}G_{xz}^{(k)}\mathbf{Z}_{\boldsymbol{\gamma}}^{(\mathbf{k})}\right)dA\cdot\mathbf{B}^{\mathbf{e}}dx\cdot\mathbf{u}^{\mathbf{e}}\end{aligned} \tag{23}$$

where $\mathbf{Z}_{\mathbf{N}}^{\mathbf{e}}\equiv\int_A\left[E_x^{(k)}\mathbf{Z}_{\boldsymbol{\varepsilon}}^{(\mathbf{k})}\right]dA$ and L_e is the finite element length.

Assuming that the internal axial-force resultant, N_x, can be approximated as the integral over the beam cross-section of the linear component of the axial stress (refer to Eqs. (8) and (5))

$$\begin{aligned}N_x &\cong\int_A E_x^{(k)}u_{x,x}dA\\ &=\int_A E_x^{(k)}\mathbf{Z}_{\boldsymbol{\varepsilon}}^{(\mathbf{k})}(z)\boldsymbol{\omega}(x)dA=\int_A E_x^{(k)}\mathbf{Z}_{\boldsymbol{\varepsilon}}^{(\mathbf{k})}(z)\mathbf{B}^{\mathbf{e}}(x)\mathbf{u}^{\mathbf{e}}dA\\ &=\int_A E_x^{(k)}\mathbf{Z}_{\boldsymbol{\varepsilon}}^{(\mathbf{k})}(z)dA\mathbf{B}^{\mathbf{e}}(x)\mathbf{u}^{\mathbf{e}}=\mathbf{Z}_{\mathbf{N}}^{\mathbf{e}}\mathbf{B}^{\mathbf{e}}(x)\mathbf{u}^{\mathbf{e}}\end{aligned} \tag{23a}$$

Eq. (23) can be rewritten as follows

$$\begin{aligned}\delta U \cong \delta\mathbf{u}^{\mathbf{e}T}\int_0^{L_e}\mathbf{B}^{\mathbf{e}T}\cdot\int_A\left(\mathbf{Z}_{\boldsymbol{\varepsilon}}^{(\mathbf{k})T}E_x^{(k)}\mathbf{Z}_{\boldsymbol{\varepsilon}}^{(\mathbf{k})}\right)dA\cdot\mathbf{B}^{\mathbf{e}}dx\cdot\mathbf{u}^{\mathbf{e}}+\frac{1}{2}\int_0^{L_e}\delta N_x\cdot\left[\mathbf{u}^{\mathbf{e}T}\mathbf{B}^{\mathbf{e}T}\mathbf{H}\mathbf{B}^{\mathbf{e}}\right]dx\cdot\mathbf{u}^{\mathbf{e}}\\ +\int_0^{L_e}\delta N_x\cdot\left[\mathbf{u}^{*\mathbf{e}T}\mathbf{B}^{*\mathbf{e}T}\mathbf{B}^{\mathbf{e}}\right]dx\cdot\mathbf{u}^{\mathbf{e}}+\delta\mathbf{u}^{\mathbf{e}T}\int_0^{L_e}\left[\mathbf{B}^{\mathbf{e}T}\mathbf{H}\mathbf{B}^{\mathbf{e}}\right]\cdot N_x dx\cdot\mathbf{u}^{\mathbf{e}}\\ +\delta\mathbf{u}^{\mathbf{e}T}\int_0^{L_e}\left[\mathbf{B}^{\mathbf{e}T}\mathbf{B}^{*\mathbf{e}}\right]\cdot N_x dx\cdot\mathbf{u}^{*\mathbf{e}}+\delta\mathbf{u}^{\mathbf{e}T}\int_0^{L_e}\mathbf{B}^{\mathbf{e}T}\cdot\int_A\left(\mathbf{Z}_{\boldsymbol{\gamma}}^{(\mathbf{k})T}G_{xz}^{(k)}\mathbf{Z}_{\boldsymbol{\gamma}}^{(\mathbf{k})}\right)dA\cdot\mathbf{B}^{\mathbf{e}}dx\cdot\mathbf{u}^{\mathbf{e}}\end{aligned} \tag{23bis}$$

Some terms can be collected thus leading to the following expression

$$\begin{aligned}\delta U \cong \delta\mathbf{u}^{\mathbf{e}T}\int_0^{L_e}\mathbf{B}^{\mathbf{e}T}\cdot\int_A\left(\mathbf{Z}_{\boldsymbol{\varepsilon}}^{(\mathbf{k})T}E_x^{(k)}\mathbf{Z}_{\boldsymbol{\varepsilon}}^{(\mathbf{k})}\right)dA\cdot\mathbf{B}^{\mathbf{e}}dx\cdot\mathbf{u}^{\mathbf{e}}+\frac{3}{2}\delta\mathbf{u}^{\mathbf{e}T}\int_0^{L_e}\left[\mathbf{B}^{\mathbf{e}T}\mathbf{H}\mathbf{B}^{\mathbf{e}}\mathbf{u}^{\mathbf{e}}\right]\cdot\mathbf{Z}_{\mathbf{N}}^{\mathbf{e}}\mathbf{B}^{\mathbf{e}}dx\cdot\mathbf{u}^{\mathbf{e}}\\ +2\delta\mathbf{u}^{\mathbf{e}T}\int_0^{L_e}\left[\mathbf{B}^{\mathbf{e}T}\mathbf{B}^{*\mathbf{e}}\mathbf{u}^{*\mathbf{e}}\right]\cdot\mathbf{Z}_{\mathbf{N}}^{\mathbf{e}}\mathbf{B}^{\mathbf{e}}dx\cdot\mathbf{u}^{\mathbf{e}}+\delta\mathbf{u}^{\mathbf{e}T}\int_0^{L_e}\mathbf{B}^{\mathbf{e}T}\cdot\int_A\left(\mathbf{Z}_{\boldsymbol{\gamma}}^{(\mathbf{k})T}G_{xz}^{(k)}\mathbf{Z}_{\boldsymbol{\gamma}}^{(\mathbf{k})}\right)dA\cdot\mathbf{B}^{\mathbf{e}}dx\cdot\mathbf{u}^{\mathbf{e}}\end{aligned} \tag{24}$$

The virtual work of external forces in the case of loads distributed along the element span is

$$\delta L_e \cong \delta\mathbf{u}^{\mathbf{e}T}\mathbf{f}^{\mathbf{e}} \tag{25}$$

where $\mathbf{f}^{\mathbf{e}}$ is the element consistent load vector corresponding to distributed loads of Eq. (14) and is defined as

$$\mathbf{f}^{\mathbf{e}}=\int_0^{L_e}\widehat{\mathbf{N}}^T\mathbf{q}dx \tag{26}$$

The matrix $\widehat{\mathbf{N}}$ is composed by the first three rows of the shape-function matrix $\mathbf{N}$ of Eq. (20), and $\mathbf{q}\equiv\begin{bmatrix}p & q & m\end{bmatrix}^T$.

Substituting Eqs. (24) and (25) into the PVW statement, Eq. (9), the element-level nonlinear equilibrium equation can be obtained

$$\mathbf{K}^{\mathbf{e}}\mathbf{u}^{\mathbf{e}}+\frac{3}{2}\overline{\mathbf{K}_{\mathbf{G}}^{\mathbf{e}}}(\mathbf{u}^{\mathbf{e}})\cdot\mathbf{u}^{\mathbf{e}}+\overline{\mathbf{K}_{\mathbf{G}}^{*\mathbf{e}}}(\mathbf{u}^{*\mathbf{e}})\cdot\mathbf{u}^{\mathbf{e}}=\mathbf{f}^{\mathbf{e}} \tag{27}$$

where the linear stiffness matrix, $\mathbf{K}^{\mathbf{e}}$, and the geometric stiffness matrices, $\overline{\mathbf{K}_{\mathbf{G}}^{\mathbf{e}}}(\mathbf{u}^{\mathbf{e}})$ and $\overline{\mathbf{K}_{\mathbf{G}}^{*\mathbf{e}}}(\mathbf{u}^{*\mathbf{e}})$, are defined as

$$\mathbf{K}^{\mathbf{e}}\equiv\int_0^{L^e}\mathbf{B}^{\mathbf{eT}}\boldsymbol{\Delta}\mathbf{B}^{\mathbf{e}}dx,\quad \overline{\mathbf{K}_{\mathbf{G}}^{\mathbf{e}}}(\mathbf{u}^{\mathbf{e}})\equiv\int_0^{L_e}\mathbf{B}^{eT}\mathbf{H}\mathbf{B}^{\mathbf{e}}\mathbf{u}^{\mathbf{e}}\mathbf{Z}_{\mathbf{N}}^{\mathbf{e}}\mathbf{B}^{\mathbf{e}}dx,\quad \overline{\mathbf{K}_{\mathbf{G}}^{*\mathbf{e}}}(\mathbf{u}^{*\mathbf{e}})\equiv\int_0^{L_e}\mathbf{B}^{eT}\mathbf{B}^{*\mathbf{e}T}\mathbf{u}^{*\mathbf{e}T}\mathbf{Z}_{\mathbf{N}}^{\mathbf{e}}\mathbf{B}^{\mathbf{e}}dx \tag{28}$$

The matrix $\overline{\mathbf{K}_{\mathbf{G}}^{\mathbf{e}}}(\mathbf{u}^{\mathbf{e}})$ is associated to the nonlinearities and it is function of the nodal degrees of freedom, while $\overline{\mathbf{K}_{\mathbf{G}}^{*\mathbf{e}}}(\mathbf{u}^{*\mathbf{e}})$ is dependent on the initial geometric imperfections.

If the internal axial-force resultant N_x is constant along the beam and corresponding to the externally applied compressive force N_0 ($N_x=-N_0$), the quantity δN_x in Eq. (23bis) vanishes and Eq. (27) becomes

$$\left(\mathbf{K}^{\mathbf{e}}-N_0\mathbf{K}_{\mathbf{G}}^{\mathbf{e}}\right)\mathbf{u}^{\mathbf{e}}=N_0\mathbf{K}_{\mathbf{G}}^{*\mathbf{e}}\mathbf{u}^{*\mathbf{e}}+\mathbf{f}^{\mathbf{e}} \tag{29}$$

where $\mathbf{K}_{\mathbf{G}}^{\mathbf{e}}$ and $\mathbf{K}_{\mathbf{G}}^{*\mathbf{e}}$ are no more dependent on the nodal-degrees of freedom and on the initial imperfections, respectively

$$\mathbf{K}_{\mathbf{G}}^{\mathbf{e}}\equiv\int_0^{L_e}\mathbf{B}^{\mathbf{eT}}\mathbf{H}\mathbf{B}^{\mathbf{e}}dx,\quad \mathbf{K}_{\mathbf{G}}^{*\mathbf{e}}\equiv\int_0^{L^e}\mathbf{B}^{eT}\mathbf{B}^{*\mathbf{e}T}dx \tag{30}$$

Buckling loads can be evaluated for symmetrically laminated beams without initial geometric imperfections by using the Euler's method of the adjacent equilibrium configurations. Considering that the beams remain straight in the pre-buckling state, the linearized stability equations can be obtained from Eq. (29)

$$\left(\mathbf{K}^{e} - N_0 \mathbf{K}_{G}^{e}\right)\hat{\mathbf{u}}^{e} = \mathbf{0} \tag{31}$$

where $\hat{\mathbf{u}}^{e}$ are incremental with respect to the pre-buckling state. Eq. (31) defines an eigenvalue problem providing both buckling loads and the corresponding buckling shapes.

4. Numerical results

The accuracy of the nonlinear model based on RZT for the analysis of multilayered beams has been assessed through a set of numerical test cases. Both critical loads of perfect beams and nonlinear static response of initially imperfect beams have been investigated. The focus of these numerical results is on sandwich beams with different core materials and slenderness ratios. Comparison with Timoshenko Beam Theory (TBT) results are also presented, as well as with high-fidelity FEM results based on commercial codes and used as benchmarks.

4.1 Beams geometry, materials, boundary conditions and applied loads

Three sandwich beams have been considered with symmetric lay-up (Table 1): two facesheets with thickness h_f and a core with thickness h_c. The width of the cross-section is b and the length of the beam is L.

Table 1. Sandwich beams geometry.

Beam	L (mm)	b (mm)	h_c (mm)	h_f (mm)
IG_32_5	320.00	48.53	6.07	5.00
WF_32_5	320.00	48.18	6.10	5.00
IG_96_2	960.00	72.40	19.93	2.00

Beams IG_32_5 and WF_32_5 share the same nominal geometry (slenderness ratio 20 and face-to-core thickness ratio 0.82) but they have a different face-to-core stiffness ratio. Beam IG_96_2 has a higher slenderness ratio (40) and a higher core-to-face thickness ratio (10).

Facesheets are made of a 7075 aluminum alloy (Ergal®) whereas cores are made of Rohacell® structural foams. Two types of foams have been used, namely WF110 and IG31. Material properties have been evaluated with a dedicated experimental tests campaign for a previous research activity [31], Table 2.

Table 2. Materials mechanical properties.

Material	E (MPa)	G (MPa)
Ergal®	69,570	25,766
Rohacell® IG31	40.3	12.4
Rohacell® WF110	196	65.4

Both cantilevered (CF) and simply-supported (SS) boundary conditions have been considered. A compressive load is applied at the beam end that is free to move axially.

[insert Figure 5.]

4.2 Models

Sandwich beams have been analyzed using beam finite elements based on both RZT and TBT. The beam length has been divided into 40 elements, found to guarantee convergence[2]. Both RZT and TBT elements formulation is based on anisoparametric interpolation (refer to Section 3 and to [24] for further details). Moreover, a shear correction factor has been used within TBT analysis that is based on the transverse-shear strain energy [32].

High-fidelity FE models based on commercial codes have also been used in order to provide reference results with high accuracy. Both Abaqus® and MSC/Nastran® have been adopted. Plane stress analyses have been performed using S4R and QUAD4 elements, respectively. The detailed description of the mesh for the considered beams is reported in Table 3.

Table 3. Mesh details for the FEM analyses performed with commercial codes.

	No. of nodes	No. of elements			
		along the beam length	along h_f	along h_c	total
(IG/WF)_32_5	5457	320	5	6	5120
IG_96_2	25947	960	2	20	23040

The compressive force is simulated as a distributed load over the cross-section of the beam. The load in each layer (per unit length of the thickness coordinate) is proportional to the corresponding

[2] The criterion adopted to determine the number of finite elements in the TBT and RZT analyses is as follows: a mesh with more than 40 elements provides negligible improvements (<1%) to the evaluation of the 1st and 2nd buckling loads of any of the considered beams. Similarly, increasing the number of elements for the nonlinear static response analyses does not lead to appreciable differences in the load-displacement response curves.

Young modulus in order to make the cross-section move remaining flat and to avoid local effects (that neither RZT and TBT could model).

4.3 Buckling loads

The first two buckling loads have been evaluated for the different combinations of beam stacking sequences and boundary conditions, Tables 4-6. The RZT solution has been obtained solving the eigenvalue problem associated to Eq. (31). An analogous solution has been obtained with the TBT. The value of the shear correction factor adopted within TBT analysis is also reported for each case.

Table 4. First two buckling loads of the IG_32_5 sandwich beam. Loads are expressed in N.

BCs	RZT	TBT (k^2=1.1163 x 10^{-3})	ABAQUS
CF	9,905	9,159	9,850
	26,856	13,196	26,292
SS	17,681	12,346	17,361
	38,980	13,522	37,745

Table 5. First two buckling loads of the WF_32_5 sandwich beam. Loads are expressed in N.

BCs	RZT	TBT (k^2=5.7162 x 10^{-3})	ABAQUS
CF	19,540	19,409	19,498
	64,303	55,153	63,985

SS	45,311	42,828	45,005
	81,329	61,332	80,009

Table 6. First two buckling loads of the IG_96_2 sandwich beam. Loads are expressed in N.

BCs	RZT	TBT (k^2=1.4914 x 10^{-2})	ABAQUS
CF	5,026	5,025	5,017
	16,076	15,994	15,973
SS	11,946	11,926	11,894
	18,354	18,162	18,172

The Refined Zigzag Theory is highly accurate in predicting the first two buckling loads for the considered beams. The more challenging problem is associated with the IG_32_5 beam that is characterized by a slenderness ratio of 20, by thick facesheets and a weak core. Nevertheless, the maximum error on the critical load is below 2% with respect to the Abaqus solution and the maximum error on the second critical load is around 3%. Beam WF_32_5 has a stiffer core and beam IG_96_2 is more slender, therefore lower errors are experienced.

A similar trend is exhibited by the Timoshenko Beam Theory, however higher discrepancies are shown with respect to the Abaqus reference solution. The critical load is evaluated with a good accuracy for beams WF_32_5 and IG_96_2, whereas it is heavily underestimated (30% error) for the simply supported IG_32_5 beam. Higher errors are found for the second buckling load of both IG_32_5 and WF_32_5 beams. It is interesting that, for the same beam, the buckling loads of the simply supported boundary conditions are less accurate with respect to the cantilevered configuration.

As already highlighted in other works [25], although an ad hoc shear correction factor is adopted, TBT is not accurate for the analysis of sandwich structures with high face-to-core thickness ratio and face-to-core stiffness ratio. And this applies also to the buckling analysis.

4.4 Nonlinear static response analysis

The nonlinear static response of initially imperfect sandwich beams subjected to a compressive load has been analyzed using different approaches to introduce the imperfection.

At first, a cantilevered IG_32_5 beam has been modeled in MSC/Patran® as a slightly-curved beam to reproduce the geometric initial imperfection. The geometric imperfection is described by the following expression

$$w^*(x) = \frac{L^2 + \mu^2 - \sqrt{(L^2 + \mu^2)^2 - 4\mu^2 x^2}}{2\mu} \tag{32}$$

In particular, the beam axis is not straight but is a circumference arc and the maximum imperfection is manifested at the beam tip, $w^*(x = L) = \mu = 1\,\text{mm}$. The same mesh details reported in Table 3 are valid for the mesh of the imperfect beam. The RZT nonlinear response has been obtained by solving Eq. (29) at different axial load levels, N_0. An analogous solution is adopted for the TBT. Figure 6 shows the load-tip deflection curve as computed using MSC/Nastran® and the TBT and RZT FE solutions[3].

[insert Figure 6.]

[3] The MSC/NASTRAN® nonlinear static response (SOL 106) has been obtained using the modified Newton's method with 10 load increments, a maximum number of 25 iterations for each load increment and a convergence criterion based on both the load equilibrium residual and the work error. For further details, refer to [33].

All of the considered beam theories correctly provide a load-deflection curve that asymptotically approaches the corresponding critical load (see Table 4).

RZT confirms its accuracy for the nonlinear analysis of sandwich beams with initial geometric imperfections. The latter are correctly modeled by using the Von Kármán definition of nonlinear strains, Eq. (5).

An Abaqus® command allows the introduction of the geometric imperfections as a linear combination of selected buckling modes, thus perfect beam models have been realized and different imperfection cases have been considered for each beam without the need to modify the model. In particular, all of the considered beams have been analyzed in both the SS and CF configurations and in presence of initial imperfections corresponding to the first buckling shape, to the second buckling shape and to a linear combination of the first two shapes (70% of the first plus 30% of the second). For all the cases, the actual deviation from the straight perfect geometry has been calculated setting to 1 mm the maximum displacement of the first and second buckling mode. Figures 7-15 show the response predictions obtained using Abaqus® as well RZT and TBT[4].

[insert Figures 7a. and 7b.]

[insert Figures 8a. and 8b.]

[insert Figures 9a. and 9b.]

[insert Figures 10a. and 10b.]

[insert Figures 11a. and 11b.]

[4] The Abaqus® nonlinear static response has been obtained using the arc-length method with a maximum number of 1000 increments and a convergence criterion based on the load equilibrium residual. For further details, refer to [34].

[insert Figures 12a. and 12b.]

[insert Figures 13a. and 13b.]

[insert Figures 14a. and 14b.]

[insert Figures 15a. and 15b.]

As expected, in case of initial geometric imperfections, either as generic function (Figure 6) or as linear combination of the buckling modes (Figures 9, 12 and 15), the load-deflection curves tend asymptotically to the first buckling load. However, when the second buckling mode is assumed as initial imperfection, the load-asymptotic value is the second buckling load of the beam (see Table 4).

The deflection of the whole beam is shown in Figures 16-20 for the IG31_32_5 in case of initial imperfection as a linear combination of the buckling modes. In Figures 16 the applied load is zero, while in Figures 17-20 it corresponds, respectively, to 25%, 45%, 70% and 90% of the critical buckling load N_{cr}.

[insert Figures 16a. and 16b.]

[insert Figures 17a. and 17b.]

[insert Figures 18a. and 18b.]

[insert Figures 19a. and 19b.]

[insert Figures 20a. and 20b.]

The vertical displacements of the nodes on the beam axis of the Abaqus model are used as reference. A perfect match between RZT and Abaqus can be observed in all cases, also for high values of N_0. It is worth noting that the deformed shape tends to the first buckling mode when N_0 approaches the first buckling load, which is the asymptotic value in the corresponding load-displacement curve, as shown in Figure 9.

Figures 7-20 prove the superior capability of the RZT in predicting the nonlinear response of sandwich beams also in presence of complex initial geometric imperfections. The accuracy of the RZT load-deflection curves (Figures 7-15) and deformed shapes (Figures 16-20) is confirmed by the Abaqus results for the considered cases of beam slenderness and face-to-core stiffness and thickness ratios.

4.5 Discussion

It is remarkable that this level of accuracy is achieved by RZT at an affordable computational cost: 40 elements, 41 nodes and 164 dofs. This is possible thanks to: (1) the RZT capability to accurately take into account the transverse shear deformation and to model the cross-section distortion of laminated beams even in presence of a highly heterogeneous stacking sequence, (2) to the need of only one additional kinematic variable with respect to the TBT, and (3) to the fact that the computational cost is independent of the number of physical layers. The number of nodes required by the FE analyses performed with commercial codes is at least 5,400 (for thick beams with thick facesheets, refer to Table 3), meaning more than 10,800 dofs (two orders of magnitude more than for RZT). For more complex stacking sequences (more physical layers), the difference would be even more pronounced.

It is therefore demonstrated that RZT can be recommended as a computationally affordable and accurate model for the analysis of laminated and sandwich beams also in the nonlinear static response regime.

Conclusions

A nonlinear formulation based on the Refined Zigzag Theory (RZT) has been developed to assess the theory for the buckling and nonlinear static response analysis of multilayered composite and sandwich beams with geometric imperfections. Numerical tests have been conducted on three sandwich beams with different core materials and slenderness ratios in both simply supported and cantilever configurations. C^0-beam finite elements based on the RZT and on the Timoshenko Beam Theory (TBT) have been employed for the analyses, and the initial imperfection within each element has been approximated by quadratic Lagrange polynomials. The RZT and TBT results have been compared to the solutions of high-fidelity commercial codes (Abaqus and Nastran) used as benchmarks.

Firstly, perfect beams have been considered to evaluate the first and the second buckling loads. The RZT error of the critical buckling load with respect to the corresponding Abaqus solution is always below 2%. Moreover, RZT is much more accurate than TBT for beams with low slenderness ratio and thicker facesheets, especially in case of higher face-to-core stiffness ratio. Then, geometric imperfections have been introduced in the models to evaluate the nonlinear response of the beams under axial compressive loads. To assess the theory for any kind of geometric imperfection, several shapes have been considered as initial deviation from the straight perfect geometry. As first case, the IG31_32_5 beam in cantilever boundary conditions has been analyzed assuming a circumference-arc shape as imperfection; the reference 2D model has been realized in Nastran. Furthermore, all the beams have been analyzed in Abaqus in both the SS and CF configurations and with initial imperfections corresponding to the first buckling shape, to the second buckling shape and to a linear combination of the first two shapes (70% of the first plus 30% of the second). The

results have shown a very good agreement between the RZT and commercial codes solutions for the evaluation of the nonlinear load-displacement equilibrium path. In all cases, the level of accuracy of the RZT is remarkable also for applied loads close to the critical buckling values, proving the superior capability of the RZT in predicting the response of sandwich beams also in presence of complex geometric nonlinearities.

The combination of high accuracy and low computational cost (only one kinematic variable more than for TBT and a number of dofs that is at least two orders of magnitude less than for high-fidelity FE models based on commercial codes) demonstrate that RZT is strongly advisable as an analysis tool for composite and sandwich beams. The results obtained in the present paper confirm this observation and extend its applicability also to the buckling and nonlinear analysis of geometrically imperfect sandwich beams.

Appendix A

In Eq. (6), the strain components dependence on the z-coordinate is expressed through the matrices

$$\mathbf{Z}_{\varepsilon}^{(k)} = \begin{bmatrix} 1 & 0 & 0 & 0 & z & \phi^{(k)} \end{bmatrix}$$

$$\mathbf{Z}_{\gamma}^{(k)} = \begin{bmatrix} 0 & 1 & 1 & \beta^{(k)} & 0 & 0 \end{bmatrix}$$

whereas $\mathbf{H}$ is the zero-one matrix

$$\mathbf{H} = \begin{bmatrix} 0 & 0 & 0 & 0 & 0 & 0 & 0 \\ 0 & 1 & 0 & 0 & 0 & 0 & 0 \\ 0 & 0 & 0 & 0 & 0 & 0 & 0 \\ 0 & 0 & 0 & 0 & 0 & 0 & 0 \\ 0 & 0 & 0 & 0 & 0 & 0 & 0 \\ 0 & 0 & 0 & 0 & 0 & 0 & 0 \end{bmatrix}$$

The matrix $\mathbf{\Delta}$ containing the stiffness coefficient in the nonlinear constitutive equations (Eq.15) is

$$\mathbf{\Delta}=\begin{bmatrix} A_{11} & 0 & 0 & 0 & B_{12} & B_{13} \\ 0 & \overline{G}A & \overline{G}A & \left(G-\overline{G}\right)A & 0 & 0 \\ 0 & \left(G-\overline{G}\right)A & \left(G-\overline{G}\right)A & \left(\overline{G}-G\right)A & 0 & 0 \\ B_{12} & 0 & 0 & 0 & D_{11} & D_{12} \\ B_{13} & 0 & 0 & 0 & D_{12} & D_{22} \end{bmatrix}$$

where

$$\left[A_{11},B_{12},D_{11}\right]\equiv\int_A E_x^{(k)}\left[1,z,z^2\right]dA$$

$$\left[B_{13},D_{12},D_{22}\right]\equiv\int_A E_x^{(k)}\phi^{(k)}\left[1,z,\phi^{(k)}\right]dA$$

$$\overline{G}\equiv\frac{1}{2h}\int_{-h}^{+h}G_{xz}^{(k)}dz$$

Appendix B

The strain–displacement matrix, $\mathbf{B}^{\mathbf{e}}$, for the two-node, eight-dof *constrained anisoparametric* element is given by [24]:

$$\mathbf{B}^{\mathbf{e}}=\frac{1}{L^e}\begin{bmatrix} N_{1,\xi}^L & 0 & 0 & 0 & N_{2,\xi}^L & 0 & 0 & 0 \\ 0 & N_{1,\xi}^L & -\alpha\frac{L_e}{8}N_{m,\xi}^Q & -\alpha c\frac{L_e}{8}N_{m,\xi}^Q & 0 & N_{2,\xi}^L & \alpha\frac{L_e}{8}N_{m,\xi}^Q & \alpha c\frac{L_e}{8}N_{m,\xi}^Q \\ 0 & 0 & L_eN_1^L & 0 & 0 & 0 & L_eN_2^L & 0 \\ 0 & 0 & 0 & L_eN_1^L & 0 & 0 & 0 & L_eN_2^L \\ 0 & 0 & N_{1,\xi}^L & 0 & 0 & 0 & N_{2,\xi}^L & 0 \\ 0 & 0 & 0 & N_{1,\xi}^L & 0 & 0 & 0 & N_{2,\xi}^L \end{bmatrix}$$

and the matrix $\mathbf{B}^{*e}$, containing the derivatives with respect to the x-coordinate of the Lagrange parabolic polynomials, is

$$\mathbf{B}^{*e} = \frac{1}{L^e}\begin{bmatrix} 0 & 0 & 0 \\ N^Q_{1,\xi} & N^Q_{m,\xi} & N^Q_{2,\xi} \\ 0 & 0 & 0 \\ 0 & 0 & 0 \\ 0 & 0 & 0 \\ 0 & 0 & 0 \end{bmatrix}$$

where $\xi \equiv 2x / L^e - 1$ is the non-dimensional axial coordinate ($\xi \in [-1,1]$ and $x \in [0, L^e]$).

References

1. AERO Magazine. *4*, http://www.boeing.com/commercial/aeromagazine/articles/qtr_4_06/AERO_Q406_article4.pdf (2006).
2. Brush DO and Almroth BO. *Buckling of bars, plates, and shells*. New York: McGraw-Hill, 1975.
3. Barbero EJ and Raftoyiannis IG. Euler buckling of pultruted composite columns. *Compos Struct* 1993; 24: 139-147.
4. De Faria AR and De Almeida SFM. Enhancement of pre-buckling behavior of composite beams with geometric imperfections using piezoelectric actuators. *Compos Part B- Eng* 1999; 30: 43-50.
5. Emam SA and Nayfeh AH. Postbuckling and free vibrations of composite beams. *Compos Struct* 2009; 88: 636-642.

6. Khdeir AA and Reddy JN. Buckling of cross-ply laminated beams with arbitrary boundary conditions. *Compos Struct* 1997; 37: 1-3.

7. Li ZM and Qiao P. Buckling and postbuckling behavior of shear deformable anisotropic laminated beams with initial geometric imperfections subjected to axial compression. *Eng Struct* 2015; 85: 277-292.

8. Bouderba B, Houari MSA, Tounsi A, et al. Thermal stability of functionally graded sandwich plates using a simple shear deformation theory. *Struct Eng Mech* 2016; 58: 397-422.

9. Bousahla AA, Benyoucef S, Tounsi A, et al. On thermal stability of plates with functionally graded coefficient of thermal expansion. *Struct Eng Mech* 2016; 60: 313-335.

10. Chikh A, Tounsi A, Hebali H, et al. Thermal buckling analysis of cross-ply laminated plates using a simplified HSDT. *Smart Struct Syst* 2017; 19: 289-297.

11. Attia A, Tounsi A, Bedia EAA, et al. Free vibration analysis of functionally graded plates with temperature-dependent properties using various four variable refined plate theories. *Steel Compos Struct* 2015; 18: 187-212.

12. Besseghier A, Houari MSA, Tounsi A, et al. Free vibration analysis of embedded nanosize FG plates using a new nonlocal trigonometric shear deformation theory. *Smart Struct Syst* 2017; 19: 601-614.

13. Bouderba B, Houari MSA and Tounsi A. Thermomechanical bending response of FGM thick plates resting on winkler-pasternak elastic foundations. *Steel Compos Struct* 2013; 14: 85-104.

14. Tounsi A, Houari MSA and Benyoucef S. A refined trigonometric shear deformation theory for thermoelastic bending of functionally graded sandwich plates. *Aerosp Sci Technol* 2013; 24: 209-220.

15. Zidi M, Tounsi A, Houari MSA, et al. Bending analysis of FGM plates under hygro-thermo-mechanical loading using a four variable refined plate theory. *Aerosp Sci Technol* 2014; 34: 24-34.

16. Beldjelili Y, Tounsi A and Mahmoud SR. Hygro-thermo-mechanical bending of S-FGM plates resting on variable elastic foundations using a four-variable trigonometric plate theory. *Smart Struct Syst* 2016; 18: 755-786.

17. Bessaim A, Houari MSA, Tounsi A, et al. A new higher-order shear and normal deformation theory for the static and free vibration analysis of sandwich plates with functionally graded isotropic face sheets. *J Sandwich Struct Mater* 2013; 15: 671-703.

18. Belabed Z, Houari MSA, Tounsi A, et al. An efficient and simple higher order shear and normal deformation theory for functionally graded material (FGM) plates. *Compos Part B-Eng* 2014; 60: 274-283.

19. Hebali H, Tounsi A, Houari MSA, et al. New Quasi-3D Hyperbolic Shear Deformation Theory for the Static and Free Vibration Analysis of Functionally Graded Plates. *J Eng Mech* 2014; 140: 374-383.

20. Sheinman I and Adan M. Effect of shear deformation on post-buckling behavior of laminated beams. *J Appl Mech* 1987; 54: 558-562.

21. Tessler A, Di Sciuva M and Gherlone M. A refined zigzag beam theory for composite and sandwich beams. *J Compos Mater* 2009; 43: 1051-1081.

22. Tessler A, Di Sciuva M and Gherlone M. A consistent refinement of first-order shear deformation theory for laminated composite and sandwich plates using improved zigzag kinematics. *J Mech Mater Struct* 2010; 5: 341-367.

23. Tessler A, Di Sciuva M and Gherlone M. A homogeneous limit methodology and refinements of computationally efficient zigzag theory for homogeneous, laminated composite, and sandwich plates. *Numer Methods Partial Differ Equ* 2011; 27: 208-229.

24. Gherlone M, Tessler A and Di Sciuva M. C0 beam elements based on the refined zigzag theory for multilayered composite and sandwich laminates. *Compos Struct* 2011; 93: 2882-2894.

25. Iurlaro L, Gherlone M, Di Sciuva M, et al. Assessment of the Refined Zigzag Theory for bending, vibration, and buckling of sandwich plates: A comparative study of different theories. *Compos Struct* 2013; 106: 777-792.

26. Iurlaro L, Gherlone M and Di Sciuva M. Bending and free vibration analysis of functionally graded sandwich plates using the Refined Zigzag Theory. *J Sandwich Struct Mater* 2014; 16: 669-699.

27. Reddy JN. Generalization of two-dimensional theories of laminated composite plates. *Commun Appl Num Methods* 1987; 3: 173-180.

28. Lu X and Liu D. An interlaminar shear stress continuity theory for both thin and thick composite laminates. *J Appl Mech* 1992; 59: 502-509.

29. Di Sciuva M. Development of an anisotropic, multilayered, shear-deformable rectangular plate element. *Comput Struct* 1985; 21: 789-796.

30. Cho M and Parmerter RR. Efficient higher order composite plate theory for general lamination configurations. *AIAA J* 1993; 31: 1299-1306.

31. Iurlaro L, Ascione A, Gherlone M, et al. Free vibration analysis of sandwich beams using the Refined Zigzag Theory: an experimental assessment. *Meccanica* 2015; 50: 2525-2535.

32. Madabhusi-Raman P and Davalos JF. Static shear correction factor for laminated rectangular beams. *Compos Part B- Eng* 1996; 27: 285-293.

33. *MD/MSC Nastran reference guide.* Santa Ana, California: MSC Software Corporation, 2010.

34. *Abaqus Analysis User's Manual*. Johnston, Rhode Island: Dassault Systèmes Simulia Corporation, 2014.

Figure Captions

Figure 1. Notation for beam geometry and applied loads.

Figure 2. Through-thickness layer notation and zigzag function of the Refined Zigzag Theory for a four-layered laminate: (a) layer notation and (b) zigzag function.

Figure 3. Nodal configuration for a two-node constrained anisoparametric element based on Refined Zigzag Theory for beams [21].

Figure 4. Parabolic approximation of the initial imperfections.

Figure 5. Load and boundary conditions: (a) simply supported beam and (b) cantilever beam under axial compressive force.

Figure 6. Load-deflection curves for the cantilevered IG_32_5 beam with initial imperfection.

Figure 7. Load-deflection curves for the IG_32_5 imperfect beam (imperfection corresponding to the 1st buckling shape): (a) CF, (b) SS.

Figure 8. Load-deflection curves for the IG_32_5 imperfect beam (imperfection corresponding to the 2nd buckling shape): (a) CF, (b) SS.

Figure 9. Load-deflection curves for the IG_32_5 imperfect beam (imperfection corresponding to a linear combination of the 1st and of the 2nd buckling shape): (a) CF, (b) SS.

Figure 10. Load-deflection curves for the WF_32_5 imperfect beam (imperfection corresponding to the 1st buckling shape): (a) CF, (b) SS.

Figure 11. Load-deflection curves for the WF_32_5 imperfect beam (imperfection corresponding to the 2nd buckling shape): (a) CF, (b) SS.

Figure 12. Load-deflection curves for the WF_32_5 imperfect beam (imperfection corresponding to a linear combination of the 1st and of the 2nd buckling shape): (a) CF, (b) SS.

Figure 13. Load-deflection curves for the IG_96_2 imperfect beam (imperfection corresponding to the 1st buckling shape): (a) CF, (b) SS.

Figure 14. Load-deflection curves for the IG_96_2 imperfect beam (imperfection corresponding to the 2nd buckling shape): (a) CF, (b) SS.

Figure 15. Load-deflection curves for the IG_96_2 imperfect beam (imperfection corresponding to a linear combination of the 1st and of the 2nd buckling shape): (a) CF, (b) SS.

Figure 16. Deflection of the IG_32_5 imperfect beam (imperfection corresponding to a linear combination of the 1st and of the 2nd buckling shape) for N_0=0: (a) CF, (b) SS.

Figure 17. Deflection of the IG_32_5 imperfect beam (imperfection corresponding to a linear combination of the 1st and of the 2nd buckling shape) for N_0=025·N_{cr}: (a) CF, (b) SS.

Figure 18. Deflection of the IG_32_5 imperfect beam (imperfection corresponding to a linear combination of the 1st and of the 2nd buckling shape) for N_0=0.45·N_{cr}: (a) CF, (b) SS.

Figure 19. Deflection of the IG_32_5 imperfect beam (imperfection corresponding to a linear combination of the 1st and of the 2nd buckling shape) for N0=0.66·Ncr: (a) CF, (b) SS.

Figure 20. Deflection of the IG_32_5 imperfect beam (imperfection corresponding to a linear combination of the 1st and of the 2nd buckling shape) for N0=0.89·Ncr: (a) CF, (b) SS.

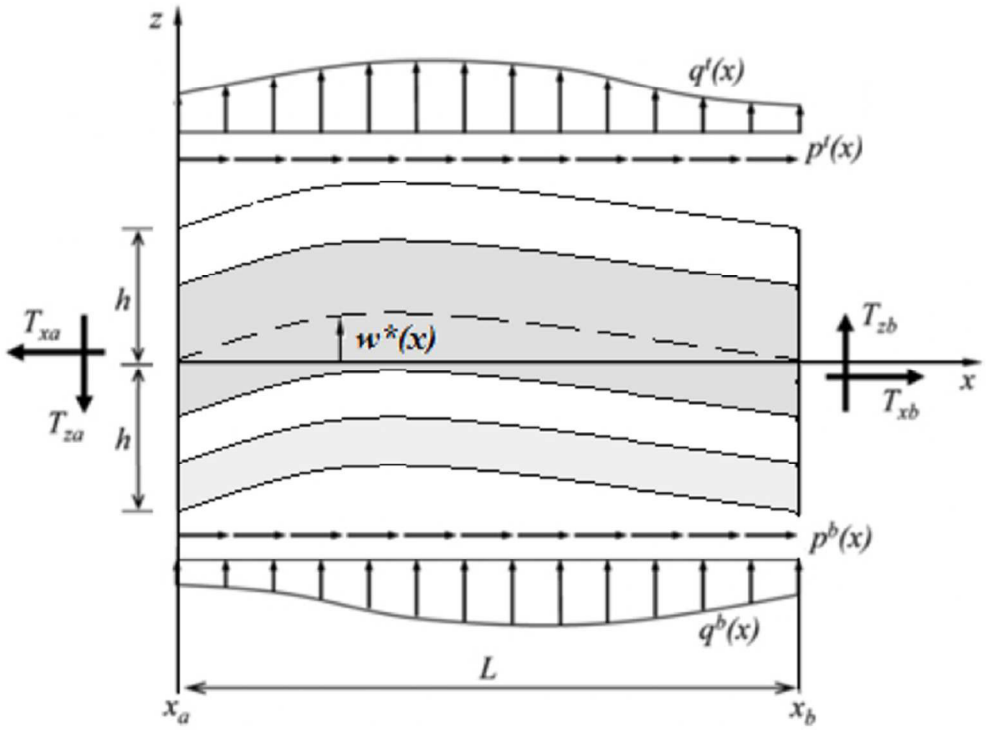

Figure 1. Notation for beam geometry and applied loads.

125x94mm (144 x 144 DPI)

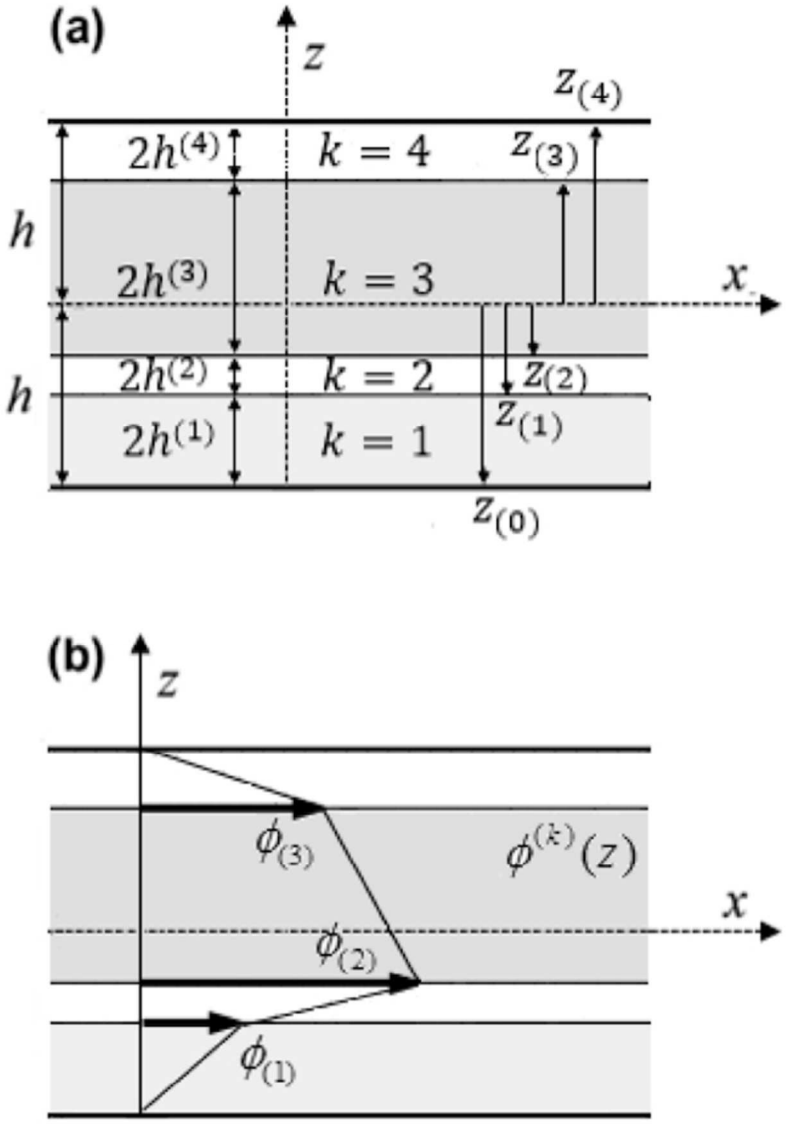

Figure 2. Through-thickness layer notation and zigzag function of the Refined Zigzag Theory for a four-layered laminate: (a) layer notation and (b) zigzag function.

119x159mm (144 x 144 DPI)

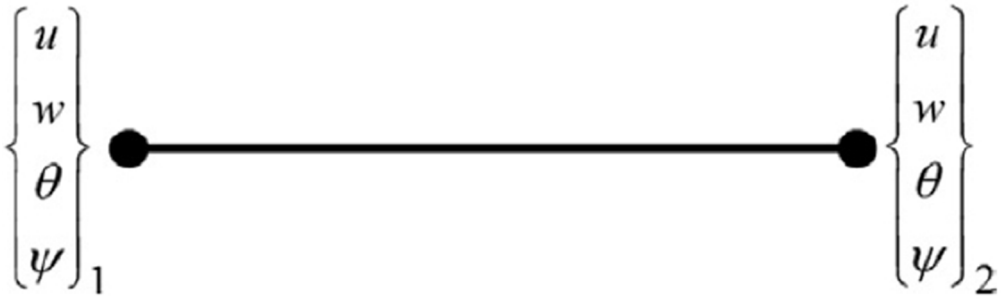

Figure 3. Nodal configuration for a two-node constrained anisoparametric element based on Refined Zigzag Theory for beams [21].

113x35mm (144 x 144 DPI)

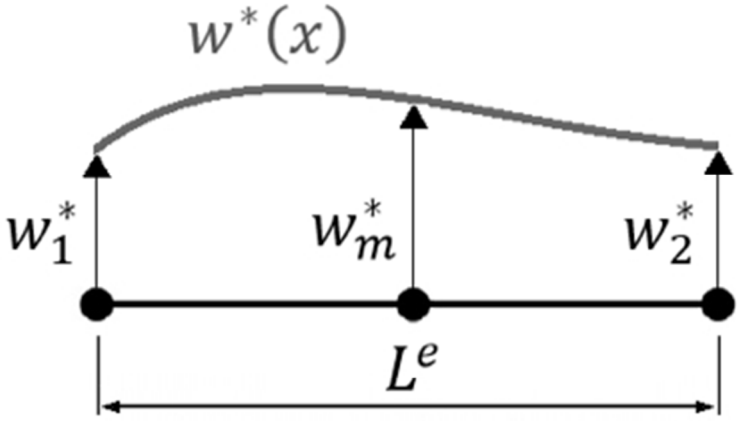

Figure 4. Parabolic approximation of the initial imperfections.

77x44mm (144 x 144 DPI)

Figure 5. Load and boundary conditions: (a) simply supported beam and (b) cantilever beam under axial compressive force.

265x51mm (144 x 144 DPI)

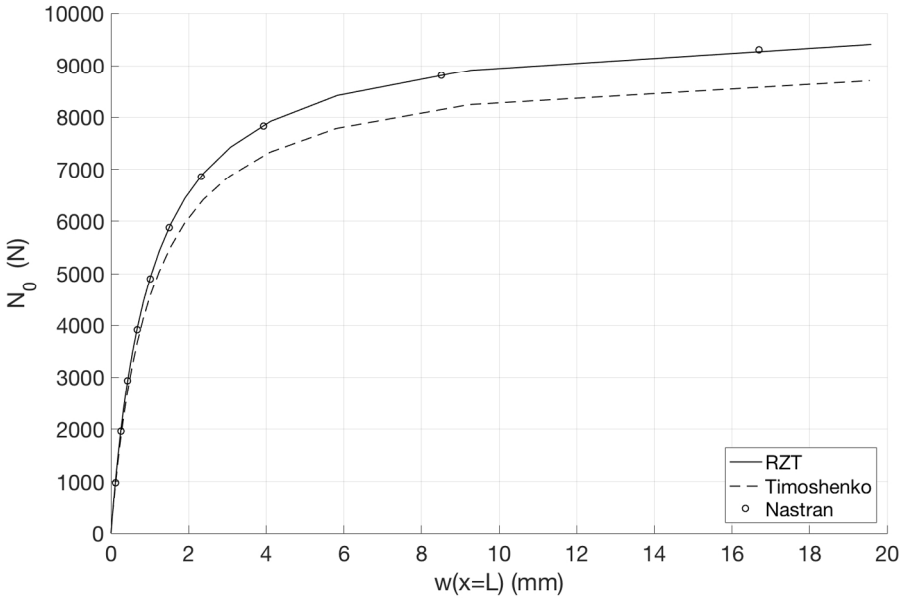

Figure 6. Load-deflection curves for the cantilevered IG_32_5 beam with initial imperfection.

651x416mm (72 x 72 DPI)

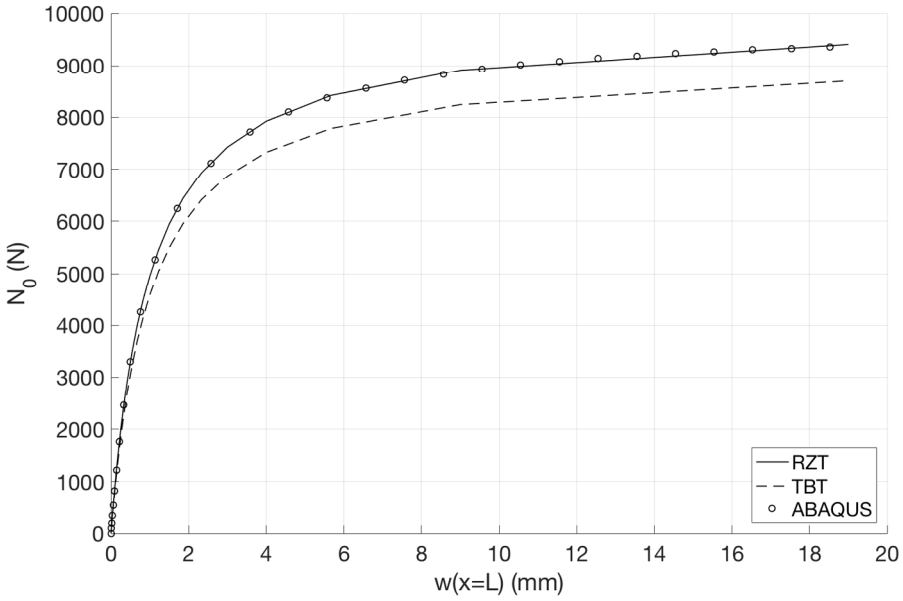

Figure 7a. Load-deflection curves for the IG_32_5 imperfect beam (imperfection corresponding to the 1st buckling shape): CF.

651x416mm (72 x 72 DPI)

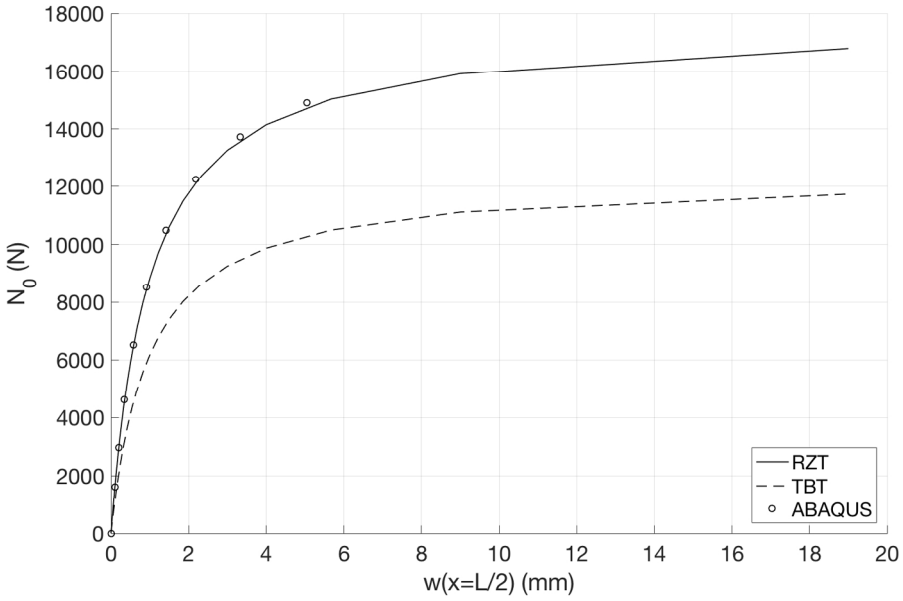

Figure 7b. Load-deflection curves for the IG_32_5 imperfect beam (imperfection corresponding to the 1st buckling shape): SS.

651x416mm (72 x 72 DPI)

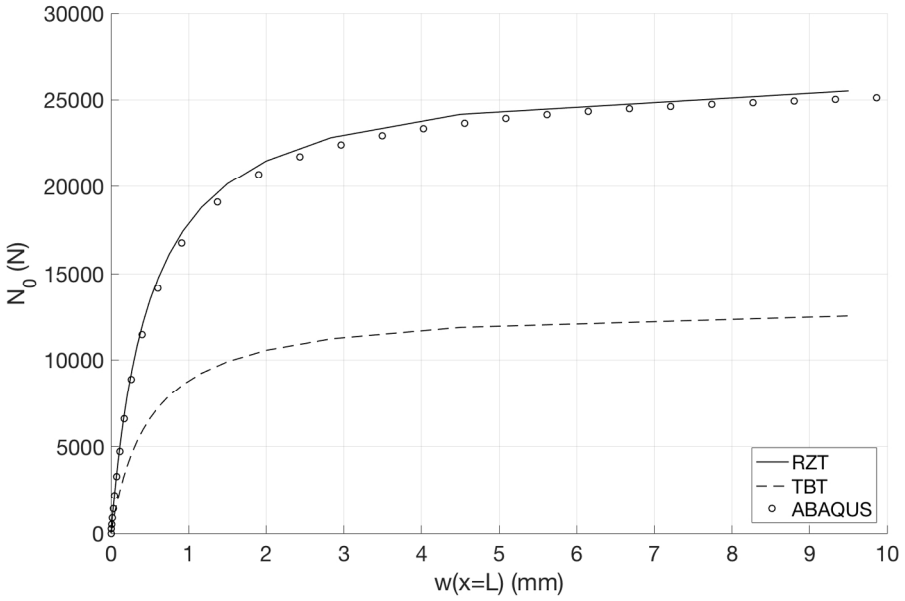

Figure 8a. Load-deflection curves for the IG_32_5 imperfect beam (imperfection corresponding to the 2nd buckling shape): CF.

651x416mm (72 x 72 DPI)

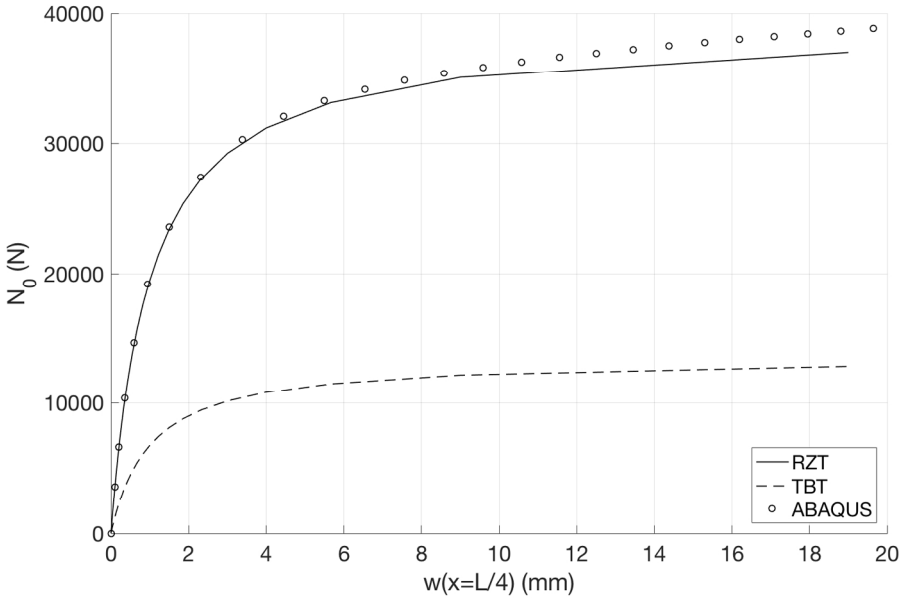

Figure 8b. Load-deflection curves for the IG_32_5 imperfect beam (imperfection corresponding to the 2nd buckling shape): SS.

651x416mm (72 x 72 DPI)

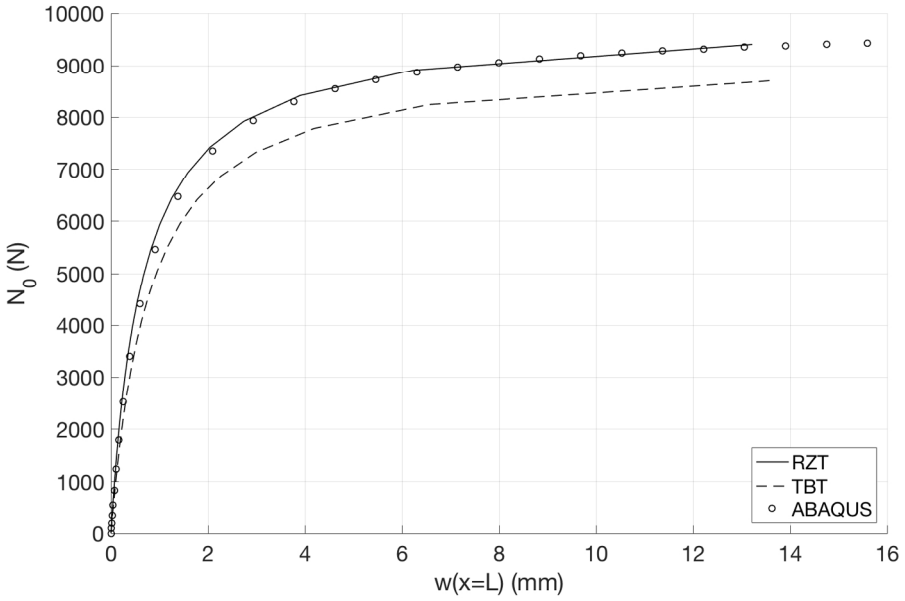

Figure 9a. Load-deflection curves for the IG_32_5 imperfect beam (imperfection corresponding to a linear combination of the 1st and of the 2nd buckling shape): CF.

651x416mm (72 x 72 DPI)

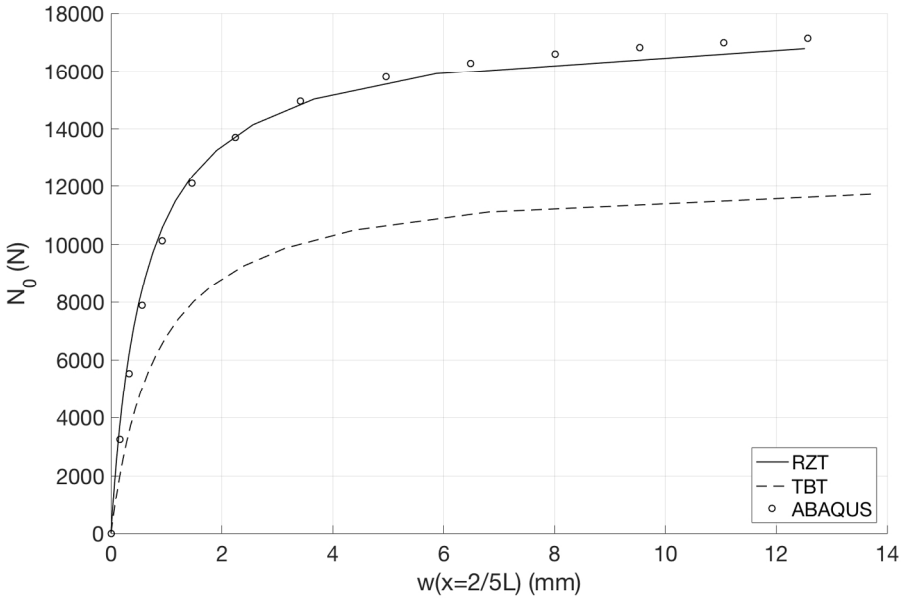

Figure 9b. Load-deflection curves for the IG_32_5 imperfect beam (imperfection corresponding to a linear combination of the 1st and of the 2nd buckling shape): SS.

651x416mm (72 x 72 DPI)

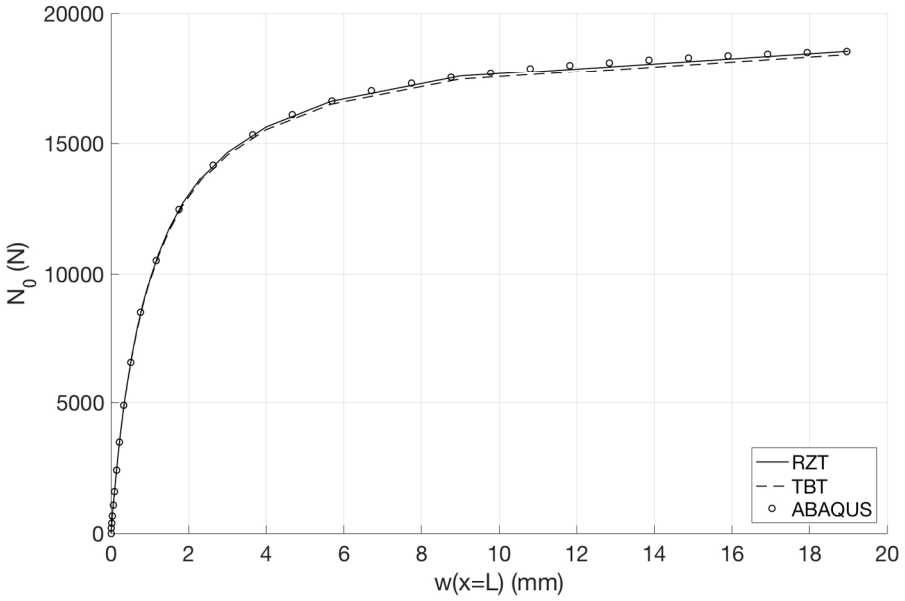

Figure 10a. Load-deflection curves for the WF_32_5 imperfect beam (imperfection corresponding to the 1st buckling shape): CF.

651x416mm (72 x 72 DPI)

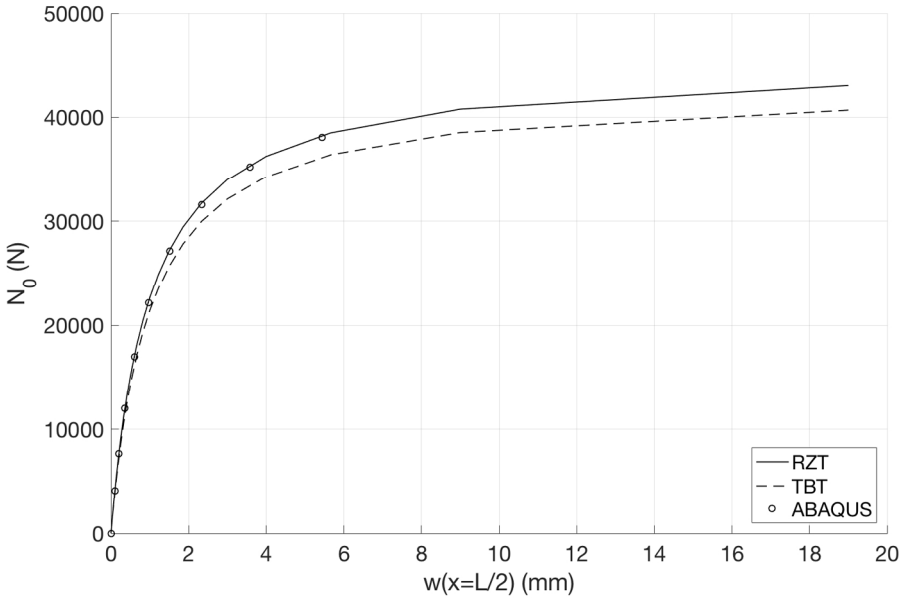

Figure 10b. Load-deflection curves for the WF_32_5 imperfect beam (imperfection corresponding to the 1st buckling shape): SS.

651x416mm (72 x 72 DPI)

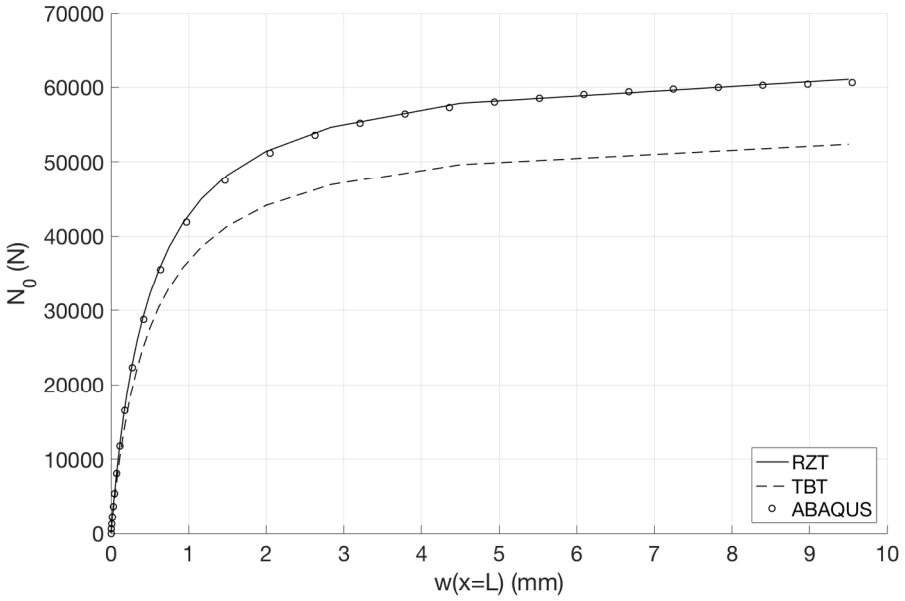

Figure 11a. Load-deflection curves for the WF_32_5 imperfect beam (imperfection corresponding to the 2nd buckling shape): CF.

651x416mm (72 x 72 DPI)

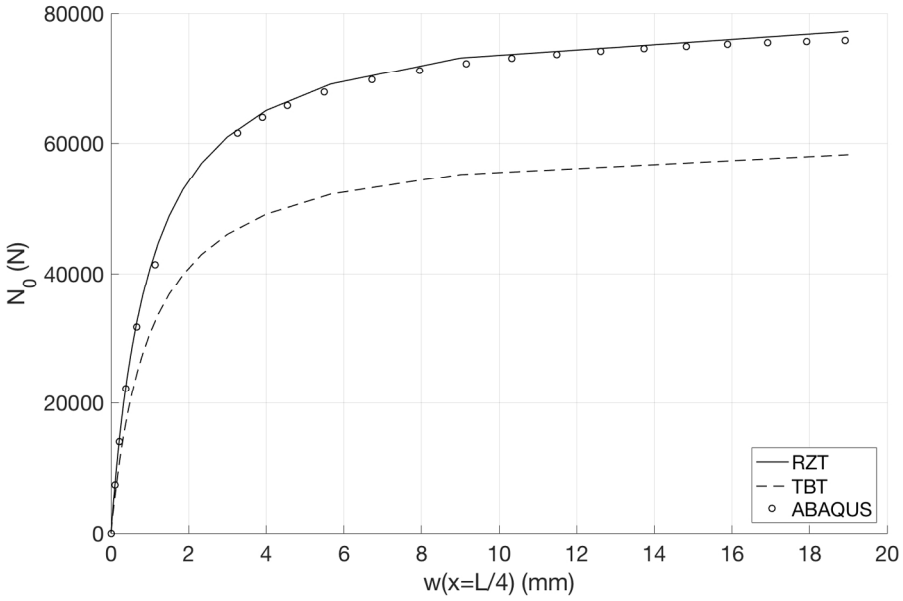

Figure 11b. Load-deflection curves for the WF_32_5 imperfect beam (imperfection corresponding to the 2nd buckling shape): SS.

651x416mm (72 x 72 DPI)

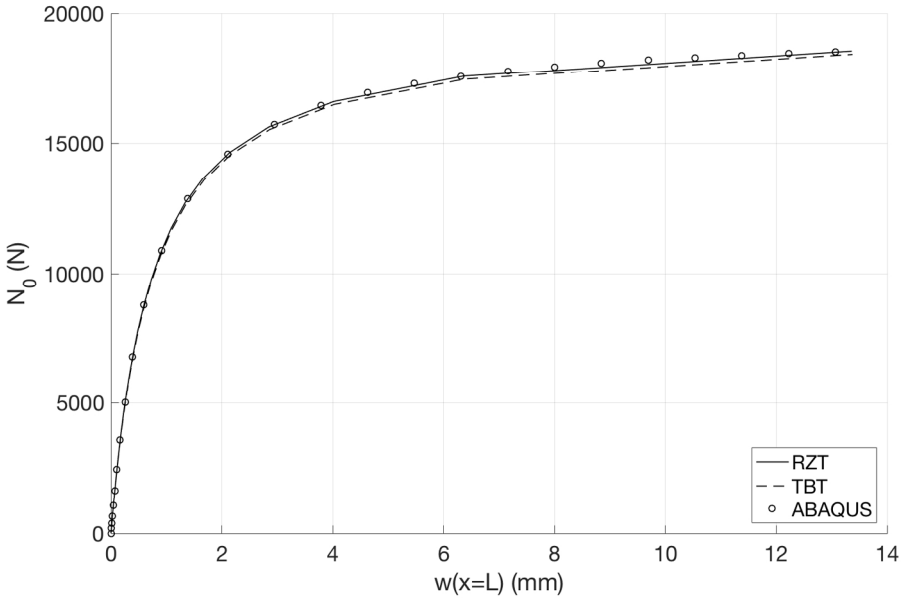

Figure 12a. Load-deflection curves for the WF_32_5 imperfect beam (imperfection corresponding to a linear combination of the 1st and of the 2nd buckling shape): CF.

651x416mm (72 x 72 DPI)

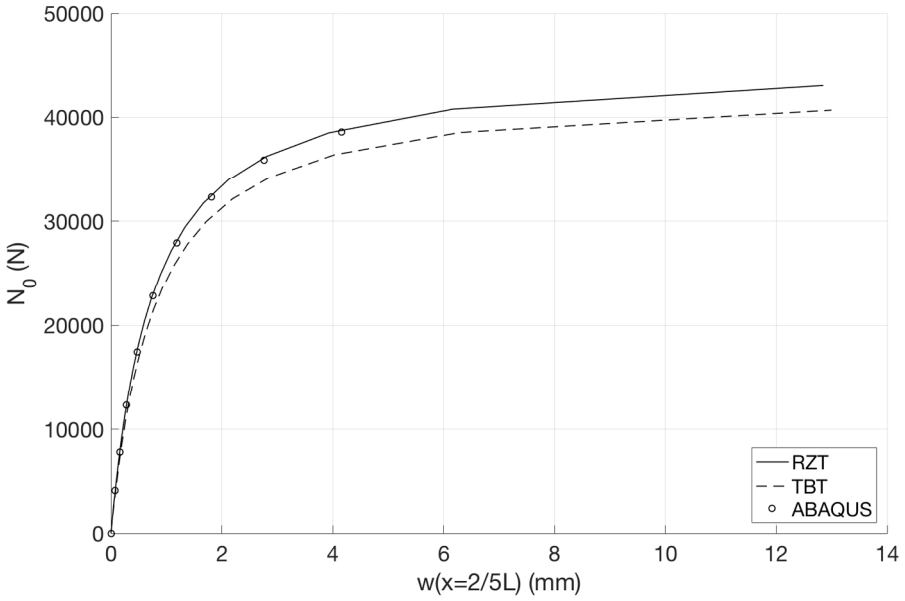

Figure 12b. Load-deflection curves for the WF_32_5 imperfect beam (imperfection corresponding to a linear combination of the 1st and of the 2nd buckling shape): SS.

651x416mm (72 x 72 DPI)

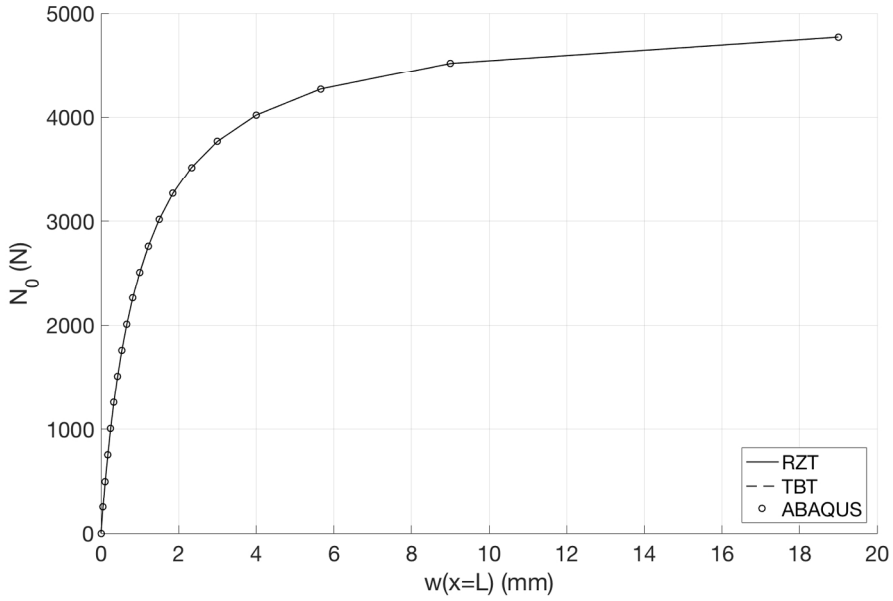

Figure 13a. Load-deflection curves for the IG_96_2 imperfect beam (imperfection corresponding to the 1st buckling shape): CF.

651x416mm (72 x 72 DPI)

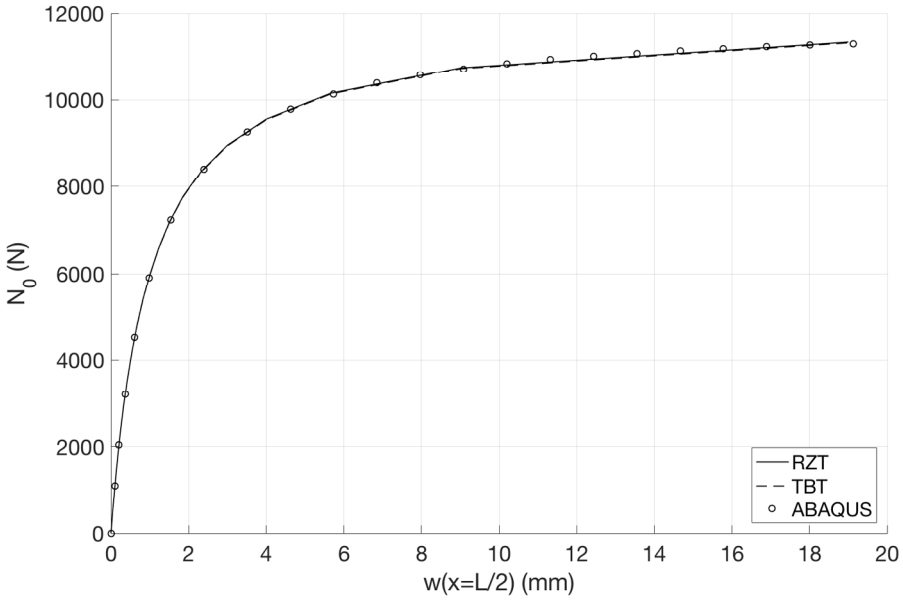

Figure 13b. Load-deflection curves for the IG_96_2 imperfect beam (imperfection corresponding to the 1st buckling shape): SS.

651x416mm (72 x 72 DPI)

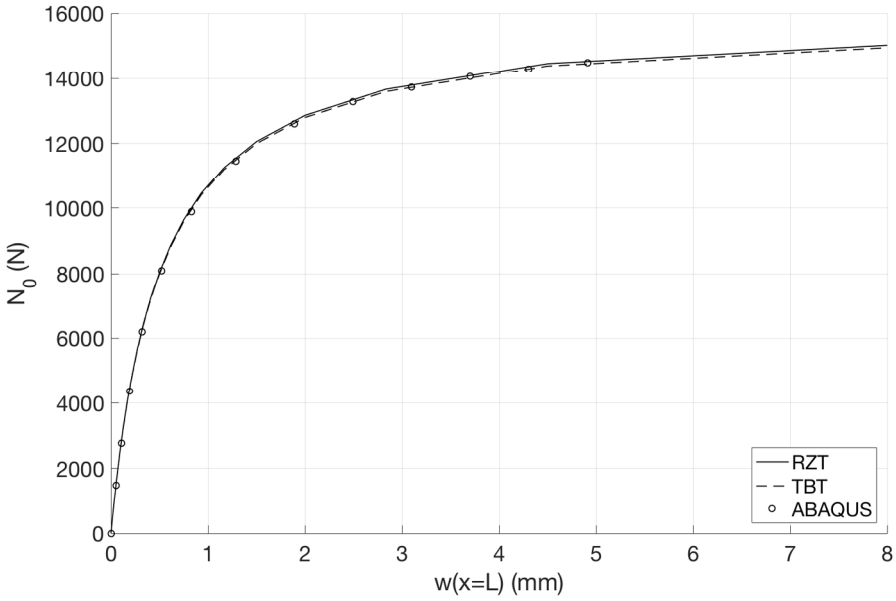

Figure 14a. Load-deflection curves for the IG_96_2 imperfect beam (imperfection corresponding to the 2nd buckling shape): CF.

651x416mm (72 x 72 DPI)

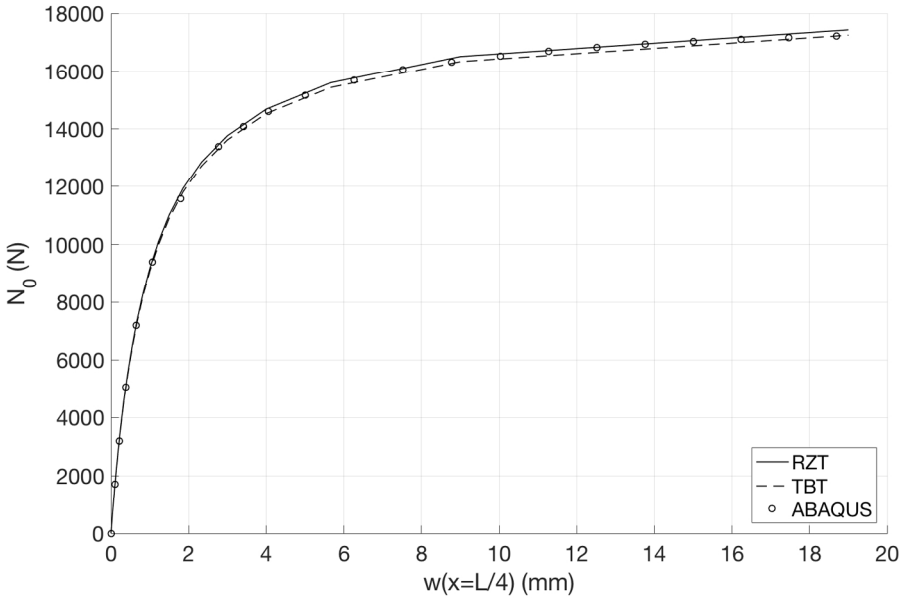

Figure 14b. Load-deflection curves for the IG_96_2 imperfect beam (imperfection corresponding to the 2nd buckling shape): SS.

651x416mm (72 x 72 DPI)

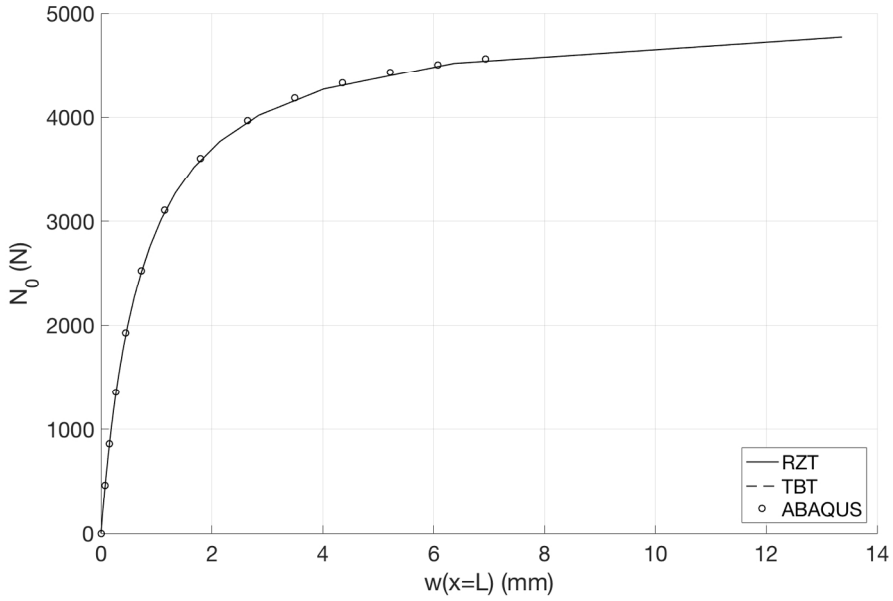

Figure 15a. Load-deflection curves for the IG_96_2 imperfect beam (imperfection corresponding to a linear combination of the 1st and of the 2nd buckling shape): CF.

651x416mm (72 x 72 DPI)

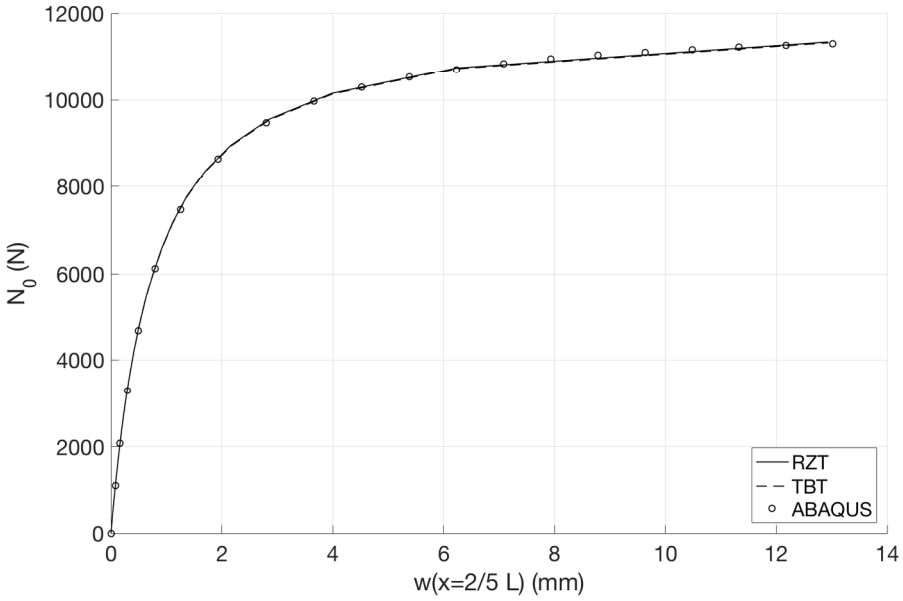

Figure 15b. Load-deflection curves for the IG_96_2 imperfect beam (imperfection corresponding to a linear combination of the 1st and of the 2nd buckling shape): SS.

651x416mm (72 x 72 DPI)

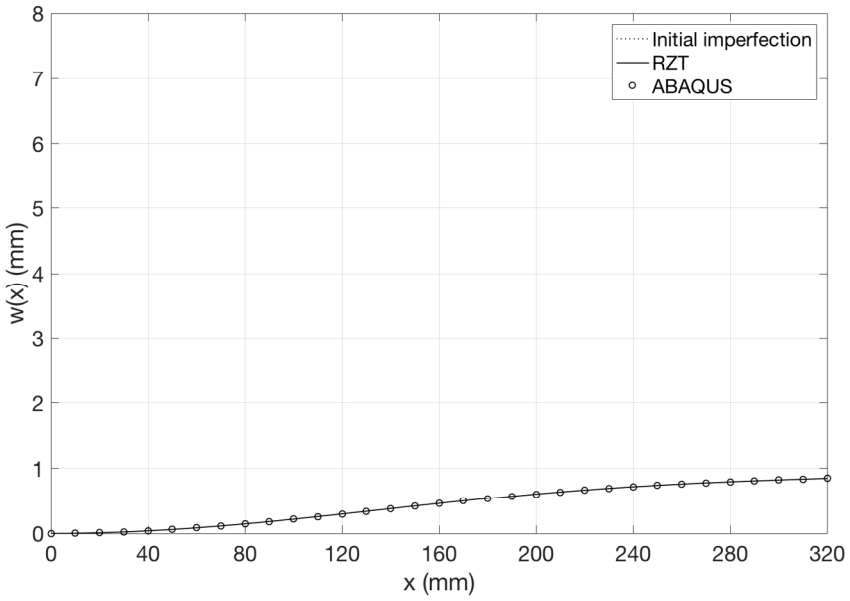

Figure 16a. Deflection of the IG_32_5 imperfect beam (imperfection corresponding to a linear combination of the 1st and of the 2nd buckling shape) for N0=0: CF.

651x416mm (72 x 72 DPI)

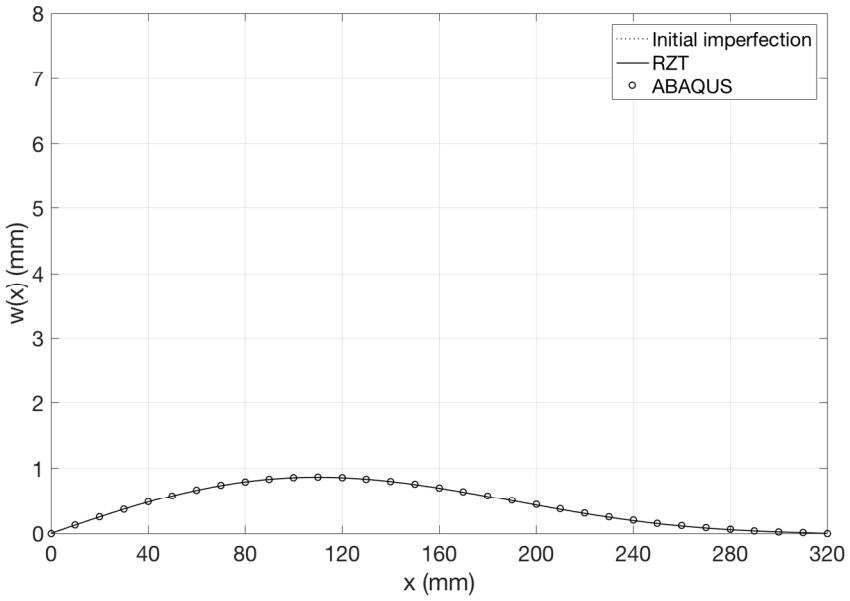

Figure 16b. Deflection of the IG_32_5 imperfect beam (imperfection corresponding to a linear combination of the 1st and of the 2nd buckling shape) for N0=0: SS.

651x416mm (72 x 72 DPI)

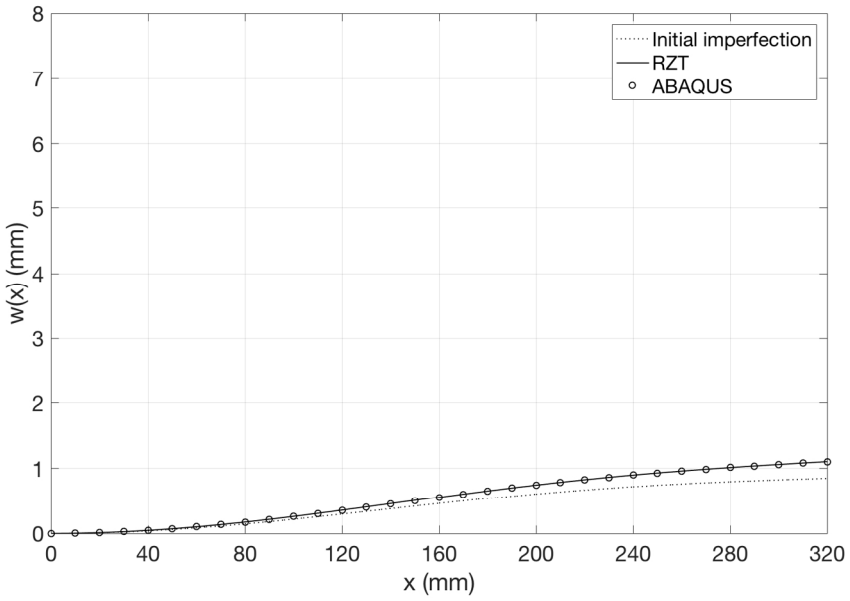

Figure 17a. Deflection of the IG_32_5 imperfect beam (imperfection corresponding to a linear combination of the 1st and of the 2nd buckling shape) for N0=025·Ncr: CF.

651x416mm (72 x 72 DPI)

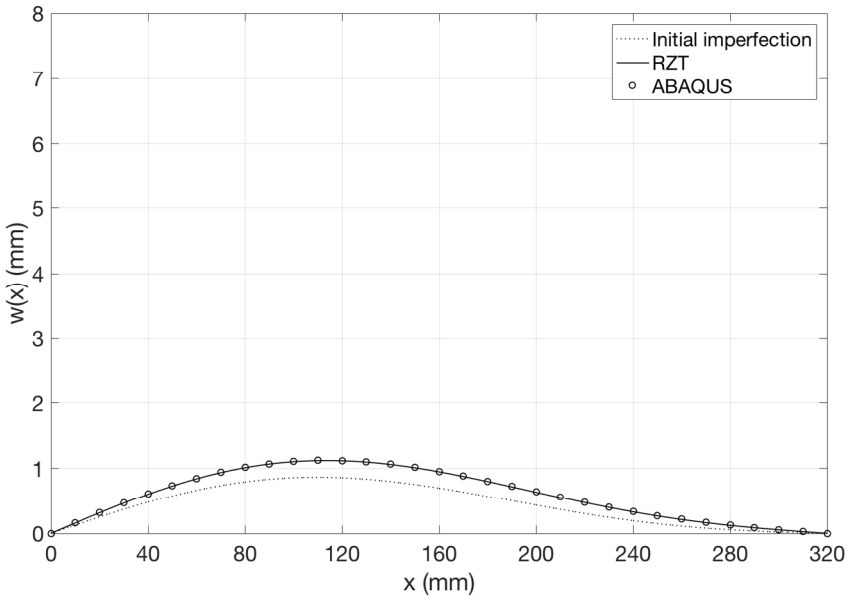

Figure 17b. Deflection of the IG_32_5 imperfect beam (imperfection corresponding to a linear combination of the 1st and of the 2nd buckling shape) for N0=025·Ncr: SS.

651x416mm (72 x 72 DPI)

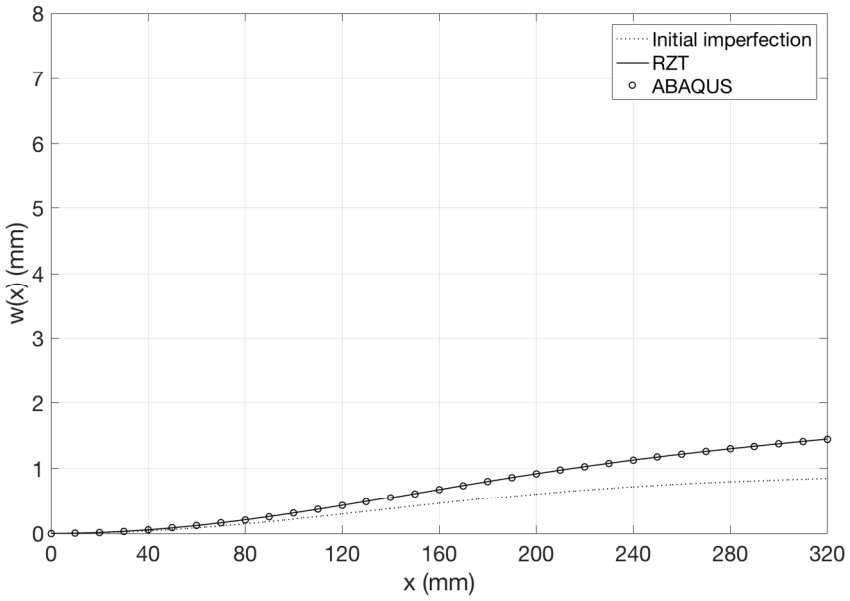

Figure 18a. Deflection of the IG_32_5 imperfect beam (imperfection corresponding to a linear combination of the 1st and of the 2nd buckling shape) for N0=0.45·Ncr: CF.

651x416mm (72 x 72 DPI)

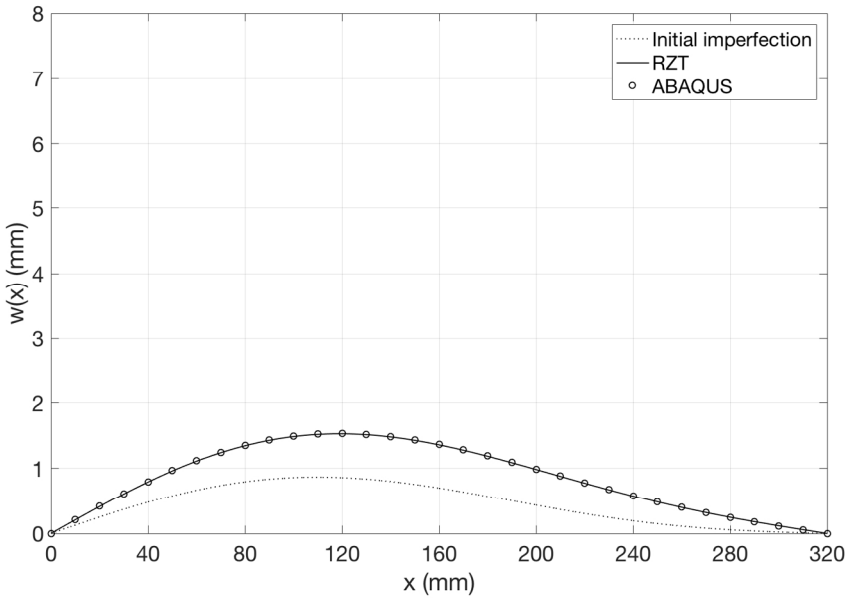

Figure 18b. Deflection of the IG_32_5 imperfect beam (imperfection corresponding to a linear combination of the 1st and of the 2nd buckling shape) for N0=0.45·Ncr: SS.

651x416mm (72 x 72 DPI)

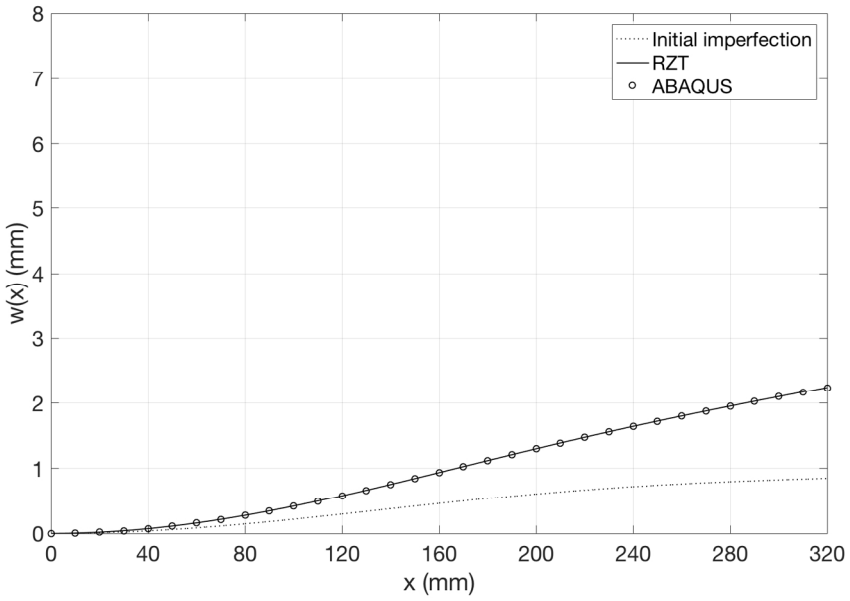

Figure 19a. Deflection of the IG_32_5 imperfect beam (imperfection corresponding to a linear combination of the 1st and of the 2nd buckling shape) for N0=0.66·Ncr: CF.

651x416mm (72 x 72 DPI)

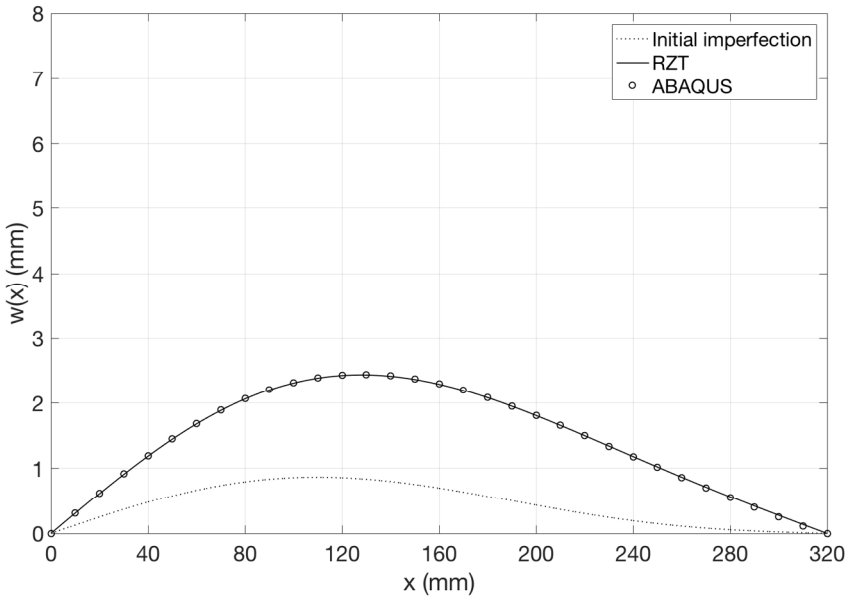

Figure 19b. Deflection of the IG_32_5 imperfect beam (imperfection corresponding to a linear combination of the 1st and of the 2nd buckling shape) for N0=0.66·Ncr: SS.

651x416mm (72 x 72 DPI)

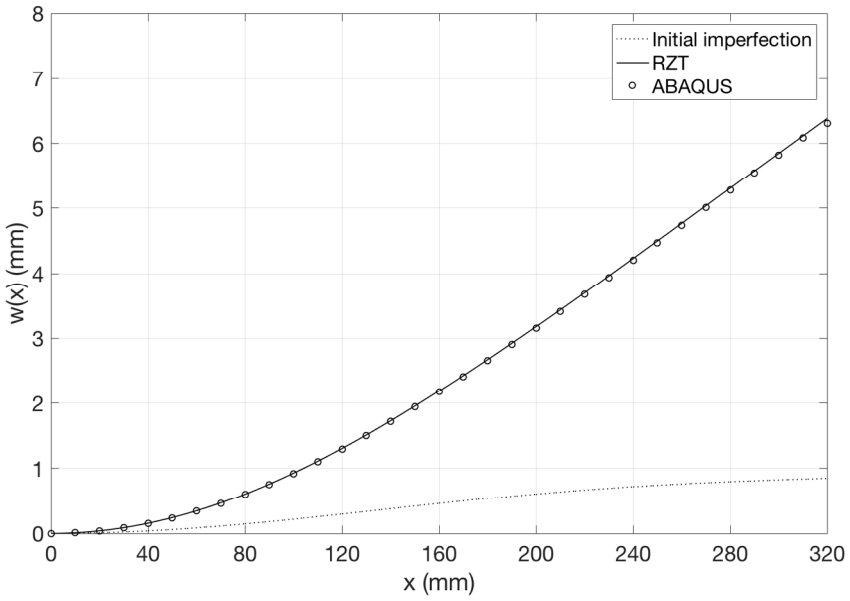

Figure 20a. Deflection of the IG_32_5 imperfect beam (imperfection corresponding to a linear combination of the 1st and of the 2nd buckling shape) for N0=0.89·Ncr: CF.

651x416mm (72 x 72 DPI)

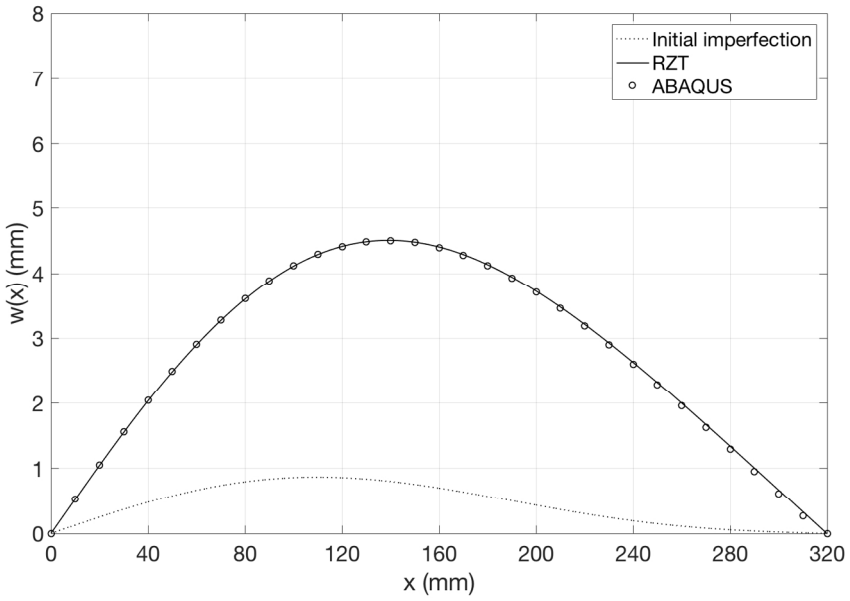

Figure 20b. Deflection of the IG_32_5 imperfect beam (imperfection corresponding to a linear combination of the 1st and of the 2nd buckling shape) for N0=0.89·Ncr: SS.

651x416mm (72 x 72 DPI)